J. Fluid Mech. (2000), *vol.* 421, *pp.* 229–267. Printed in the United Kingdom

Compressibility effects in a turbulent annular mixing layer. Part 1. Turbulence and growth rate

By JONATHAN B. FREUND†, SANJIVA K. LELE AND PARVIZ MOIN

Center for Turbulence Research, Stanford University, Stanford, CA 94305, USA

(Received 11 November 1997 and in revised form 21 March 2000)

This work uses direct numerical simulations of time evolving annular mixing layers, which correspond to the early development of round jets, to study compressibility effects on turbulence in free shear flows. Nine cases were considered with convective Mach numbers ranging from $M_c = 0.1$ to 1.8 and turbulence Mach numbers reaching as high as $M_t = 0.8$.

Growth rates of the simulated mixing layers are suppressed with increasing Mach number as observed experimentally. Also in accord with experiments, the mean velocity difference across the layer is found to be inadequate for scaling most turbulence statistics. An alternative scaling based on the mean velocity difference across a typical large eddy, whose dimension is determined by two-point spatial correlations, is proposed and validated. Analysis of the budget of the streamwise component of Reynolds stress shows how the new scaling is linked to the observed growth rate suppression. Dilatational contributions to the budget of turbulent kinetic energy are found to increase rapidly with Mach number, but remain small even at $M_c = 1.8$ despite the fact that shocklets are found at high Mach numbers. Flow visualizations show that at low Mach numbers the mixing region is dominated by large azimuthally correlated rollers whereas at high Mach numbers the flow is dominated by small streamwise oriented structures. An acoustic timescale limitation for supersonically deforming eddies is found to be consistent with the observations and scalings and is offered as a possible explanation for the decrease in transverse lengthscale.

1. Introduction

There are several technologies in which compressible mixing plays a critical role and which would benefit both from improved models and better understanding of the physical processes in compressible turbulence (see a recent review by Gutmark, Schadow & Yu 1995). The motivation of this study is to better understand fundamental properties of compressible turbulent free shear flows with an eye toward improving turbulence models for these engineering applications. Many modelling endeavours have originated in the incompressible limit and then extrapolated into the compressible regime. However, unlike compressible turbulent boundary layers, models for free shear flows have met with only limited success. It is clear that these require significant compressibility corrections before yielding reliable results (Bradshaw 1996).

† Present address: Mechanical and Aerospace Engineering, University of California, Los Angeles, USA.

Nearly all modern studies of fundamental aspects of compressible free shear flows have focused on the plane mixing layer. As pointed out by Brown & Roshko (1974), this flow has characteristics favourable for analysis which are not present in all free shear flows. Of primary importance is that the plane mixing layer maintains the same mean velocity, density and scalar concentration differences across the layer as it develops downstream. This is in contrast to a fully developed jet, for example, which has continuously varying mean centreline velocity. However, the initial shear layer development of a round jet, before the potential core closes, has also been studied with some success to understand compressibility effects in free shear flows (Fourguette, Mungal & Dibble 1991; Clemens & Paul 1995). Taking a similar approach in this study, we consider an annular mixing layer which corresponds to the early development of a jet.

Perhaps the most significant effect of compressibility on a free shear flow is a suppressed growth rate. Early experiments noting this effect are surveyed by Birch & Eggers (1972) and more recent studies (Chinzei *et al.* 1986; Papamoschou & Roshko 1988; Samimy & Elliott 1990; Fourguette *et al.* 1991; Göebel & Dutton 1991; Clemens & Mungal 1992; Hall, Dimotakis & Rosemann 1993) also all show a suppression of mixing-layer growth rate with increasing compressibility. The convective Mach number, M_c (Bogdanoff 1983; Papamoschou & Roshko 1988), which is based upon an estimated convective velocity of theoretical large flow structures, has been used with reasonable success to parameterize shear flow compressibility and is used in this work.

Numerical simulation has also been used to study compressible turbulence. Early simulations of homogeneously sheared compressible turbulence (Sarkar *et al.* 1991*a*, *b*); Blaisdell, Mansour & Reynolds 1993) found that the pressure–dilatation correlation and the dilatational dissipation were significant parts of the turbulent kinetic energy budget and that turbulence Mach number, M_t (see § A.2.3 for a definition), was a key parameter for growth rate of turbulent kinetic energy. However, in a more recent work on homogeneous shear flow, Sarkar (1995) has attributed the suppression of growth rate to the gradient Mach number, $M_g = (\ell/\bar{a})(\partial\bar{u}/\partial y)$, where ℓ is an integral scale of the turbulence and a is the sound speed. He concluded that at higher M_g the shear stress anisotropy is suppressed and consequently the production of turbulent kinetic energy is reduced. Sarkar suggested that a similar mechanism operates in a mixing layer. Taking a lead from Simone, Coleman & Mansour (1997) and Lele (1994), we will interpret M_g as a ratio of timescales and use it to interpret some of the physical results.

Taking a step toward increasingly realistic flows, Vreman, Sandham & Luo (1996) simulated turbulent temporally developing plane mixing layers at convective Mach numbers of $M_c = 0.2, 0.6, 0.8$ and 1.2. Linear instability modes were used as initial conditions and were allowed to develop into turbulence. The growth rate was suppressed with increasing M_c in a manner similar to that observed experimentally. However, in contrast to the early homogeneous shear flow simulations, dilatational effects were negligible with regard to the turbulent energetics. It was, however, found that pressure–strain-rate correlations were suppressed with increasing Mach number and this was used to explain the growth rate suppression. The present work builds upon this earlier effort. We study a similar flow and offer a more complete explanation of the compressibility effects in shear layers. Our simulations cover a wider range of convective Mach numbers and represent a better-developed turbulent flow.

An objective of this work is to help refine the basic understanding of compressible turbulent flows. Simone *et al.* (1997) divide compressible flow modelling attempts into *shape explicit* and *implicit* approaches. *Explicit* refers to modelling the dilatational

terms that appear explicitly in the turbulent kinetic energy transport equation and, thus, an assumption inherent to this approach is that the compressible terms have a significant direct effect on turbulence energetics. In the *implicit* approach, the compressibility is assumed to influence the structure of the turbulence and this in turn changes the turbulence energetics. In this case, the dilatational terms may be negligible in the turbulent kinetic energy equation. *Explicit* modelling attempts (Sarkar *et al.* 1991*b*; Zeman 1990) have had some success. However, recent results of Vreman *et al.* (1996) and the present study suggest that they may not be based upon realistic physics and *implicit* modelling appears to be more realistic. In such an attempt, Breidenthal (1990) developed the concept of a 'sonic eddy' and used it to propose a mechanism for the suppression of growth rate in mixing layers. The underlying assumption of his analysis is that eddies with Mach number difference across their extent greater than unity do not play an active role in the entrainment of fluid. Using similar reasoning, Burr & Dutton (1990) proposed a model for reduced pressure–strain-rate correlations by postulating that pressure disturbances are only likely to remain correlated with strain rates over the volume they influence within a large-eddy timescale. More recently, Vreman *et al.* (1996) modelled pressure–strain-rate correlations in terms of pressure minima and maxima which were estimated by the depressed core pressure of a sonic eddy (Breidenthal 1990) and the pressure at isentropic stagnation points.

Our study shows that the quintessential element of 'compressibility effects' is the suppression of transverse turbulent lengthscale with increasing convective Mach number. Concomitantly, the pressure fluctuations, pressure–strain-rate correlations, Reynolds stresses and shear-layer growth rate are suppressed with M_c. We provide consistent scaling for second-order statistics of turbulence fluctuations; however, this scaling does not appear to uniformly hold for each term in the budget of the Reynolds stresses for the present developing shear layer.

This paper is organized as follows. In § 2, background information concerning the flow and the simulations is presented along with some fundamental results. The scaling of key turbulence statistics is discussed in § 3 and new scalings are proposed and analysed. Analysis of the Reynolds stress transport equations in § 4 serves to link the new scaling to the growth rates, and turbulence energetics are analysed in § 5. Results and implications are discussed in § 6 and a summary is given in § 7.

2. Preliminaries

2.1. *Flow geometry*

The present study is of a streamwise periodic annular mixing layer (figure 1, which also defines the coordinate system used). Although streamwise periodic flows do not have exact laboratory counterparts, the present flow approximately corresponds to the early development of a jet as studied by Fourguette *et al.* (1991) and Clemens & Paul (1995). Simulations of a spatially developing jet are currently too expensive for parametric studies of compressibility effects.

As seen in figure 1, there are two lengthscales in the annular mixing layer which preclude a formally self-similar development prior to the potential core closing. One lengthscale is the shear-layer thickness, δ, and the other is the shear-layer radius, r_o. These lengthscales are discussed in more detail in § 2.4. The computational domain extended to $21r_o$ in x and $3.5r_o$ in r. In the numerical solution, a characteristics-based non-reflecting boundary condition was applied at $r = 3.5r_o$.

Despite obvious differences with plane mixing layers, it is shown in this paper

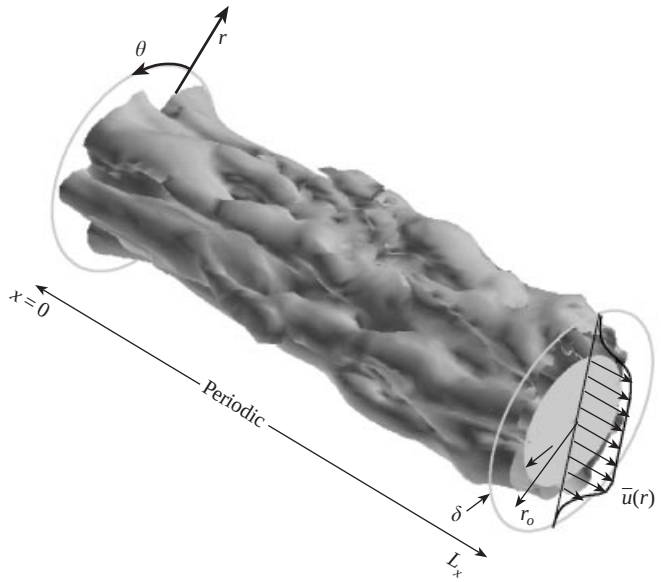

FIGURE 1. Flow schematic showing mean flow profile and coordinate system definition. The flow is depicted with an iso-surface of instantaneous axial velocity.

that many compressible plane mixing-layer results, which are far more prevalent than jet shear-layer results, apply very well to the annular flow. Most importantly, these include growth rate and Reynolds stress suppressions with increasing Mach number. It is doubtful that many flows of engineering interest strictly obey self-similar development and the present study also gives insight into cases when self-similar arguments might be used effectively.

2.2. *Governing equations and numerical method*

For the Mach number regimes considered, jet Mach number $M \leqslant 3.5$, and in the absence of strong shocks, the compressible Navier–Stokes equations govern the flow. Since the geometry is axisymmetric, it is natural to solve the equation in cylindrical coordinates (x, r, θ) with corresponding velocities v_x, v_r, and v_θ. The conservation equations in cylindrical coordinates are well known and the reader is referred to Freund, Moin & Lele (1997) for the equations in detail. To close the equations, Fourier's law was used to calculate the heat fluxes with constant Prandtl number, $Pr = 0.7$, and a perfect gas was assumed. The functional relation of viscosity to temperature was specified with Sutherland's law taking constants appropriate for air at atmospheric conditions.

In the numerical algorithm, spatial derivatives were computed with a sixth-order Padé finite-difference scheme (Lele 1992) in the axial and radial directions and with Fourier spectral methods in the azimuthal direction. There were $448 \times 146 \times 192$ mesh points in the axial, radial and azimuthal directions, respectively. The equations were integrated in time with a fourth-order Runge–Kutta algorithm.

Two types of averages are used in this study. An overbar, $\bar{f}$, indicates a Reynolds average and a tilde, $\tilde{f}$ indicates a density weighted or Favre average. Averages are taken over both x and θ. Perturbation from Reynolds averages are indicated with f' and perturbations from Favre averages are indicated with f'', hence $f = \bar{f} + f' = \tilde{f} + f''$.

Case	A	B	C	D	E	F	G	H	I
M_j	0.20	0.40	0.80	1.15	1.55	1.92	2.5	3.0	3.5
M_c	0.10	0.21	0.41	0.59	0.79	0.99	1.29	1.54	1.80
Re	2100	2250	2100	2100	2400	2500	2250	2500	3200
T_j/T_∞	1.12	1.12	1.12	1.12	1.12	1.12	1.12	1.12	1.12
δ_{m_o}/r_o	0.088	0.088	0.087	0.087	0.086	0.084	0.081	0.079	0.077
t_δ/τ_t	1.09	1.11	1.06	1.23	1.38	2.09	2.17	2.32	2.96
N_{ens}	1	4	1	1	1	10	1	1	1

TABLE 1. Parameters from all runs.

2.3. *Initial conditions and flow parameters*

The initial mean velocity was

$$\bar{v}_x(r) = \frac{U_j}{2}\left[1 - \tanh\left[\frac{1}{4b}\left(\frac{r}{r_o} - \frac{r_o}{r}\right)\right]\right], \tag{2.1}$$

where U_j was the initial centreline jet velocity and b, a thickness parameter, was 0.08 for all cases. The subscript $(\cdot)_j$ designates a centreline value. This study will focus on times before the potential core closes and thus U_j, for example, is constant. The initial mean temperature was calculated with the Crocco–Busemann relation, the initial mean pressure was constant, and $\bar{v}_r = \bar{v}_\theta = 0$.

The turbulence was initialized by adding velocity perturbations of prescribed energy spectrum and random phase to the mean flow. This was a straightforward process in the homogeneous directions, x and θ, but the radial direction is inhomogeneous and, therefore, it was not possible to initialize an exact one-dimensional spectrum in this direction. Instead, a 'pseudo-spectrum' was prescribed and modulated so that perturbations decayed rapidly to zero away from the sheared region (Freund *et al.* 1997). The amplitude of the perturbations was scaled so that

$$(\overline{v_x'v_x'} + \overline{v_r'v_r'} + \overline{v_\theta'v_\theta'})^{1/2}_{\max} = 0.05U_j. \tag{2.2}$$

Initial density and pressure fluctuations were zero. It has been demonstrated that initializing pressure and density in this way causes clear difficulties in homogeneous flows (with periodic boundary conditions) because acoustic disturbances have no means of leaving the domain (Ristorcelli & Blaisdell 1997). However, in the present study, we do not consider the data until after spurious initial disturbances have, for the most part, radiated away. There is no evidence of excessive dilatation in the results presented below.

Nine different cases were simulated and their parameters are listed in table 1. The only significant change between the different cases is the centreline Mach number, M_j, which varies from 0.2 to 3.5. The convective Mach number (Bogdanoff 1983; Papamoschou & Roshko 1988) is often used to parameterize compressibility effects and is also listed in table 1. This quantity is typically used to label the different cases. For the present flow it is defined as $M_c = U_j/(a_\infty + a_j)$ where a is the speed of sound. The Reynolds number listed in table 1 is defined in terms of centreline quantities and the initial mixing-layer radius, $Re = \rho_j r_o U_j/\mu_j$. The momentum thickness of the shear layer is defined as

$$\delta_m = \int_0^\infty \frac{\bar{\rho}\tilde{v}_x}{\rho_j U_j}\left(1 - \frac{\tilde{v}_x}{U_j}\right) r\,\mathrm{d}r \tag{2.3}$$

and its initial values are also tabulated in table 1.

Some cases were simulated repeatedly with different random phases for the initial fluctuations to provide a larger statistical sample. The number of such ensembles, N_{ens}, is listed in the last line of table 1. The first ensemble at every Mach number was simulated with identical initial velocity perturbations to offer the best possible comparisons between the cases. Ensemble averages are constructed as a simple mean.

2.4. *Flow development*

Before discussing the data we must address the fact that this flow is neither statistically stationary nor formally self-similar and therefore it is not obvious how to compare data from different runs in a meaningful way. The low- and high-Mach-number flows evolve very differently, and picking a single instant in time at which to compare results is unsatisfactory, if not incorrect. Also, there is no temporal normalization which provides obvious points of comparison. So, without any more favourable options, we chose to use the mixing-layer thickness as an indicator of flow evolution. Dimensional analysis supports this choice. Following Papamoschou & Roshko (1988), non-dimensionalization of the plane mixing-layer problem suggests the functional relation for growth rate,

$$\delta' = f\left(\frac{U_1}{U_2}, \frac{\rho_1}{\rho_2}, \frac{\gamma_1}{\gamma_2}, M_1, \frac{t}{\tau_t}\right), \tag{2.4}$$

where the subscripts indicate the two free-stream values. We have included a non-dimensional time to reflect the fact that the present flow is developing; τ_t in (2.4) is a large-eddy timescale and is discussed in § 6.3. The plane mixing layer has a single lengthscale, the thickness δ, giving rise to its well-known self-similarity and linear growth. The present flow has an additional lengthscale, r_o, the shear-layer radius. We may include the mixing-layer radius in (2.4) and assume a new functional form

$$\delta' = g\left(\frac{U_1}{U_2}, \frac{\rho_1}{\rho_2}, \frac{\gamma_1}{\gamma_2}, M_1, \frac{t}{\tau_t}, \frac{\delta}{r_o}\right). \tag{2.5}$$

By comparing the different mixing layers at the same values of δ/r_o, we effectively eliminate this parameter from the equation. There is no reason to expect that g in (2.5) is the same as f in (2.4), but in the limit of $\delta/r_o \to 0$ the plane and annular mixing layers are identical and $f = g$. This suggests that f and g are similar and, as we shall see, in many cases the annular mixing layer at a single value of δ_m/r_o behaves in a very similar fashion to the plane mixing layer.

The results in the body of the paper are all presented at the $\delta_m = 0.2r_o$ point which is approximately when the potential core is about to close. Values of t_δ/τ_t, the time at which $\delta_m = 0.2r_o$ is reached, are provided in table 1. The increase of t/τ_t with M_c reflects the decreased spreading rate (see § 2.5). Since the thickness has just more than doubled at this point, by some measures this would be in the early stage of mixing-layer development. The development of the flow up to this point is documented in Appendix A. The main conclusions of that appendix are that the mean flow develops in a nearly self-similar fashion and its mean velocity profile is insensitive to Mach number, the turbulence has realistically broadbanded spectra, and two-point correlations decay to small values within the computational box, as they must for it to be physically realistic. It is also shown that turbulence Mach number reaches as high as $M_t = 0.8$ in the $M_c = 1.8$ case and that the Reynolds stresses follow trends observed in plane mixing-layer experiments at similar Mach numbers. The streamwise micro-scale Reynolds number is $Re_{\lambda_x} > 150$ at $\delta_m = 0.2r_o$ for all the

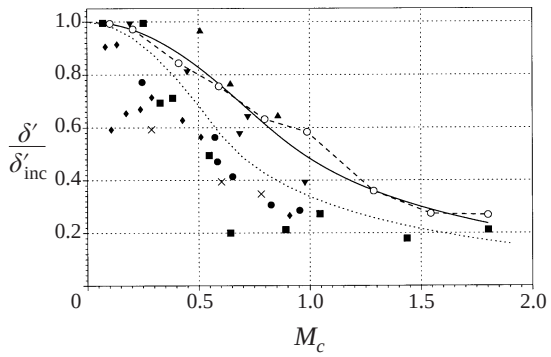

FIGURE 2. – ○ –, Momentum thickness growth rate from the simulations and growth rates from several experiments: ●, Chinzei *et al.* 1986; ■, Papamoschou & Roshko 1988; ▲, Samimy & Elliot 1990; ▼, Göebel & Dutton (1991); ◆, Hall *et al.* (1993); ×, Clemens & Mungal 1992. Also shown are linear mode maximum amplification rates normalized by their incompressible value for - - -, spatially developing plane mixing layers (Day *et al.* 1998) and ——, for the present flow.

cases and the radial micro-scale Reynolds numbers drops from $Re_{\lambda_r} = 78$ to 26 with increasing Mach number (Freund *et al.* 1997).

2.5. *Growth rate suppression*

We now consider the growth rate of the layer at $\delta_m = 0.2r_o$. An expression for the momentum thickness growth rate at an instant may be derived by time differentiating (2.3) and using equations for $\bar{\rho}\tilde{u}_x$ and $\bar{\rho}\tilde{u}_x\tilde{u}_x$:

$$\delta'_m = \frac{1}{U_j}\frac{\partial \delta_m}{\partial t} = -\frac{2}{r_o \rho_j U_j^3}\int_0^\infty \left(\bar{\rho}\widetilde{v''_x v''_r}\frac{\partial \tilde{u}_x}{\partial r} - 2\bar{\tau}_{xr}\frac{\partial \tilde{u}_x}{\partial r}\right) r\,\mathrm{d}r. \tag{2.6}$$

Vreman *et al.* (1996) derived a similar expression in Cartesian coordinates. It is exact, and by using it we avoid both finite differencing in time and making imprecise visual fits of straight lines through the data to estimate growth rates. A common practice is to present growth rate data as a function of the convective Mach number and to normalize it by a corresponding incompressible value. In this case the incompressible growth rate was estimated by quadratic extrapolation of the $M_c = 0.10$ and $M_c = 0.21$ data. Data normalized by this value and data from several experimental studies are plotted in figure 2. There is significant scatter in the experimental data but the simulation data follows the general trend of decreasing growth rate with increasing Mach number. The present simulations also capture the apparent growth rate saturation at very high convective Mach numbers observed by Papamoschou & Roshko (1988).

It is clear in figure 2 that the present growth rates are suppressed more slowly with increasing Mach number than most of the spatially developing plane mixing-layer data. This behaviour is predicted by linear stability amplification rates which have been shown to be highly correlated to spreading rates (Ragab & Wu 1990; Sandham & Reynolds 1990). The peak linear mode amplification rate calculated by Day, Reynolds & Mansour (1998) for spatially developing plane mixing layers and the peak linear mode amplification rate for the annular mixing layer when $\delta_m = 0.2r_o$ are also shown. The linear analysis predicts the overall suppression of growth rate for both geometries and that the growth of the annular mixing layer is apparently suppressed more gradually with increasing compressibility than the plane mixing layer.

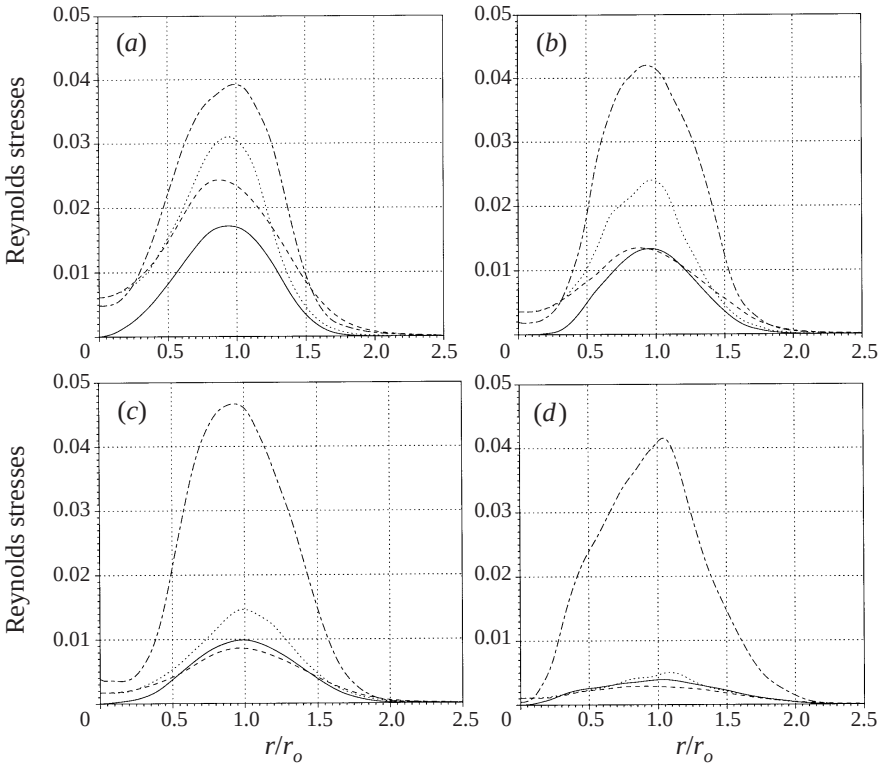

FIGURE 3. Favre averaged Reynolds stresses for the cases: (*a*) $M_c = 0.21$, (*b*) $M_c = 0.59$, (*c*) $M_c = 0.99$, (*d*) $M_c = 1.80$. —·—, $\bar{\rho}\widetilde{v_x''v_x''}/\rho_j U_j^2$; – – –, $\bar{\rho}\widetilde{v_r''v_r''}/\rho_j U_j^2$; ·····, $\bar{\rho}\widetilde{v_\theta''v_\theta''}/\rho_j U_j^2$; ——, $\bar{\rho}\widetilde{v_x''v_r''}/\rho_j U_j^2$.

3. Scaling observations

3.1. *Reynolds stresses*

The Favre averaged Reynolds stresses are given in figure 3 for four of the cases. The $M_c = 0.21$ and $M_c = 0.99$ cases were ensemble averaged. The minor bumps and asymmetries in the profiles of the other Mach number cases are attributed to insufficient statistical sample. The shear stress, $\bar{\rho}\widetilde{v_x''v_r''}$, and the radial and azimuthal normal stresses, $\bar{\rho}\widetilde{v_r''v_r''}$ and $\bar{\rho}\widetilde{v_\theta''v_\theta''}$, are clearly suppressed with increasing Mach number. However, the axial normal stress, $\bar{\rho}\widetilde{v_x''v_x''}$, is not suppressed and maintains nearly the same value (when normalized by $\rho_j U_j^2$) as the Mach number increases. The $\bar{\rho}\widetilde{v_x''v_x''}$ trend is in agreement with some experiments (Göebel & Dutton 1991; Urban & Mungal 1998) while in disagreement with others (Elliott & Samimy 1990; Samimy & Elliott 1990).

It is clear from figure 3 that the Reynolds shear stress is suppressed relative to the total kinetic energy as Mach number increases. This may be seen more clearly with the shear stress anisotropy parameter

$$b_{12} = \frac{\widetilde{v_x''v_r''}}{\widetilde{v_x''v_x''} + \widetilde{v_r''v_r''} + \widetilde{v_\theta''v_\theta''}}. \tag{3.1}$$

Figure 4(*a*) shows the shear stress anisotropy profile across the middle of the mixing region for three cases at different Mach numbers, and confirms that the shear stress

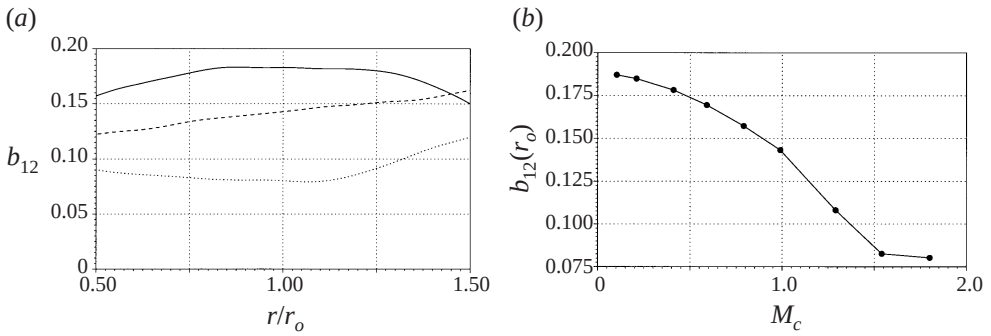

FIGURE 4. Shear stress anisotropy for (*a*) cases ——, $M_c = 0.21$; – – –, $M_c = 0.99$; ·····, $M_c = 1.80$; (*b*) all cases at $r = r_o$.

anisotropy is reduced as Mach number increases. This result is in general agreement with the homogeneous shear results of Sarkar (1995) who proposed that structural changes in turbulence at higher Mach numbers are reflected in b_{12}. Only the middle of the mixing region is shown in figure 4 because the denominator in (3.1) becomes small toward the edges of the mixing region and, consequently, b_{12} becomes poorly behaved. To better quantify the trend with Mach number, we take the shear stress anisotropy at $r = r_o$ to be a good representative value and plot it versus Mach number in figure 4(*b*). Clearly, $b_{12}(r_o)$ steadily decreases with increasing compressibility until the highest Mach number is reached. The levelling off of the curve at the highest Mach number is consistent with the growth rate also becoming relatively constant at these conditions.

3.2. *Suppression of pressure fluctuations*

It is also interesting to consider pressure fluctuations. Root-mean-squared pressure fluctuations normalized by $\rho_j U_j^2$ are plotted in figure 5 for all Mach numbers. Once again, U_j provides a poor scaling. Kraichnan (1956) showed that scale anisotropy, which here increases significantly with Mach number, could itself lead to suppressed pressure fluctuations. However, the present pressure fluctuations are suppressed well beyond his estimates, and we conclude that the suppression is a Mach-number effect rather than strictly an anisotropy effect.

3.3. *Radial lengthscale*

From the above observations, we see that turbulence statistics (with the exception of $\widetilde{\bar{\rho} v_x'' v_x''}$) do not scale with the velocity difference across the mixing layer and we now offer a structural change as a possible explanation. In contrast to low Mach numbers, where experimental visualizations clearly indicate that the large turbulent structures span the mixing layers (Brown & Roshko 1974), the transverse extent of the large eddies at higher Mach number remains unclear from experimental visualizations (Papamoschou & Roshko 1988; Clemens & Mungal 1995). If the transverse lengthscale of the large eddies, ℓ, is less than the layer thickness, δ, (with $\ell \approx \delta$ for $M \to 0$) then we should not expect the turbulence to scale with the velocity difference across the layer. Instead, it should scale with the velocity difference across a large eddy, $\sim U_j \ell / \delta$.

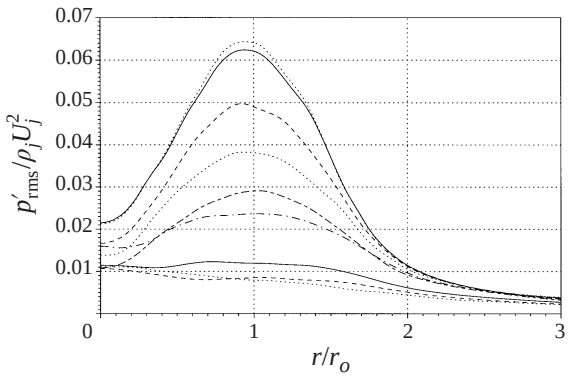

FIGURE 5. Normalized pressure fluctuation for all cases (from top to bottom): ·····, $M_c = 0.2$; ——, $M_c = 0.21$; – – –, $M_c = 0.41$; ·····, $M_c = 0.59$; — – —, $M_c = 0.79$; — · —, $M_c = 0.99$; ——, $M_c = 1.29$; – – –, $M_c = 1.54$; · · · · · ·, $M_c = 1.80$.

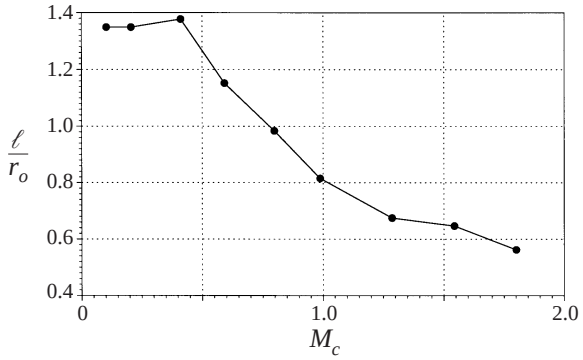

FIGURE 6. Transverse large-eddy lengthscale.

To examine this hypothesis, we define a transverse large-eddy lengthscale for the mixing layer, ℓ, in terms of the two-point correlation of radial velocity at $r = r_o$,

$$\frac{\overline{v'_r(r_o - \ell/2)v'_r(r_o + \ell/2)}}{\overline{v'_r(r_o)v'_r(r_o)}} = 0.1. \tag{3.2}$$

Figure 6 shows that there is a clear decrease in this lengthscale with increasing Mach number. Changing the threshold of 0.1 in equation (3.2) to 0.05 or 0.2 has little effect on this trend. Fluctuations at $r = r_o$ rescaled with $U_j\ell/\delta_m$ are plotted in figure 7. Clearly, the large suppression of $\overline{p'p'}$, $\overline{v'_r v'_r}$, and $\overline{v'_x v'_r}$ has been removed. Poor statistical convergence of the data is blamed for the bumpiness of the curves.

There remain, however, some questions concerning how these terms can scale as they do and be consistent with the observed growth rate. For example, the $U_j\ell/\delta$ scaling does not explain how $\overline{v'_x v'_x}/U_j^2$ can remain nearly constant while other components are suppressed; it also does not explain why $\overline{v'_x v'_r}$ should scale with $U_j^2\ell^2/\delta_m^2$ rather than $U_j^2\ell/\delta_m$ as might be expected given the $\overline{v'_x v'_x}$ scaling. In addition, we note that the growth rate does not scale with either ℓ/δ_m or ℓ^2/δ_m^2 ($[\ell/\delta_m]^{1.5}$ is perhaps the best fit but there is no physical basis for this). An analysis of the Reynolds-stress equations is necessary to understand the interrelation of these turbulence quantities and the growth rate. In the following section, it will be shown that these apparent

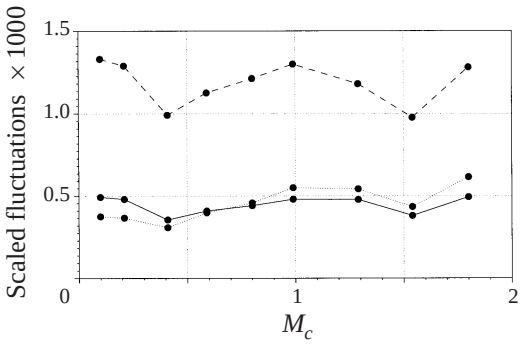

FIGURE 7. Turbulence statistics at $r = r_o$ scaled by ℓ: – – –, $p'_{\rm rms}/\bar{\rho}U_j^2(\ell/\delta_m)^2$; ——, $\overline{v'_x v'_r}/U_j^2(\ell/\delta_m)^2$; ·····, $\overline{v'_r v'_r}/U_j^2(\ell/\delta_m)^2$.

contradictions are in accord with Reynolds-stress budget terms and a link will be established between the new scaling for $\overline{p'p'}$ and the growth rate.

4. Reynolds stress transport and budgets

4.1. *Reynolds-stress transport*

Terms in the transport equations for the Reynolds stresses (see Appendix B) are calculated for the $M_c = 0.21$ and the $M_c = 0.99$ cases. The other Mach-number cases have only single realizations available for averaging which is insufficient for converged statistics. For this reason, Mach-number trends will be discussed primarily using radially integrated quantities, which are less sensitive to the sample size. These will be studied in the following sections where pressure fluctuations, and hence the new scalings, are connected to the growth rate.

To simplify expressions, several abbreviations will be used when discussing the budgets. The symbol $\mathscr{P}_{st}$ is the production term, Π_{st} is the pressure–strain-rate correlation term, and ε_{st} is the viscous dissipation term in the $\widetilde{\bar{\rho}u''_s u''_t}$ transport equation, where s and t are any of the coordinate directions x, r, or θ. Similarly, R_{st} is shorthand for $\widetilde{\bar{\rho}u''_s u''_t}$. $\mathscr{P}$ and ε without subscripts indicate the production and dissipation of turbulent kinetic energy, respectively.

Before proceeding to evaluate the terms in the Reynolds-stress transport equations, there are issues associated with the cylindrical coordinate system that need clarification. The first issue involves terms in cylindrical coordinates without analogues in Cartesian coordinates which redistribute the Reynolds stresses. They appear in the R_{rr}, $R_{\theta\theta}$, and R_{xr} equations (see Appendix B). In the R_{rr} and $R_{\theta\theta}$ equations, these terms have finite limits at the origin ($r = 0$) and therefore present no difficulty. However, in the R_{xr} equations both the cylindrical redistribution term, $\overline{\rho v''_x v''_\theta v''_\theta}/r$, and the turbulence transport term,

$$-\frac{1}{r}\frac{\partial r\overline{\rho v''_x v''_r v''_r}}{\partial r}, \tag{4.1}$$

are singular at $r = 0$. At $r = 0$, however, they are equal and opposite, and so we combine them when showing budget terms as a function of radius. Later, the cylindrical redistribution term is separated, multiplied by r to remove the singularity, and replotted. For consistency, this practice is also followed for the R_{rr} and $R_{\theta\theta}$ equations. It is clear that the cylindrical redistribution terms are not transport terms

because they do not necessarily integrate to zero across the layer. A second issue involves the pressure diffusion and pressure–strain-rate terms in the R_{xr} equation which are also singular at $r = 0$. They are recombined into the well-behaved velocity–pressure gradient term for plotting the budgets versus r/r_o and later discussed as separate terms.

Budget terms of the Reynolds-stress transport equations are plotted in figures 8–11 for the $M_c = 0.21$ and $M_c = 0.99$ cases. The profiles are qualitatively similar at the two Mach numbers, but the magnitudes at $M_c = 0.99$ are typically half those at $M_c = 0.21$. In the R_{xx} equation, the major source term is the turbulent kinetic energy production and the major sink terms are the viscous dissipation and the velocity–pressure gradient (here equal to the pressure–strain-rate). Since the pressure–dilatation correlation is very small (figure 21*b*), the pressure–strain-rate tensor is nearly trace free, and in the R_{xx} equation it acts primarily to redistribute the turbulent kinetic energy from R_{xx} to R_{rr} and $R_{\theta\theta}$. In the R_{rr} and $R_{\theta\theta}$ equations (figures 9 and 10) it is clear that the major source term is indeed the velocity–pressure-gradient which includes the pressure–strain-rate. The time rate-of-change term is significant and positive in the R_{rr} and $R_{\theta\theta}$ equations at both Mach numbers; it is also non-zero in the middle of the shear region, in contrast to the R_{xx} time rate of change.

The major source of R_{xr} is its production (figure 11) and its only significant sink term is the velocity–pressure-gradient or, equivalently, since the pressure diffusion has no net source or sink effect, the pressure–strain-rate correlation. The velocity–pressure-gradient term, $-\overline{v_r''(\partial p'/\partial x)} - \overline{v_x''(\partial p'/\partial r)}$, in the R_{xr} equation is separated into the pressure diffusion, $-(1/r)(\partial r\overline{p'v_x''}/\partial r)$, and pressure–strain-rate terms, $\overline{p'((\partial v_r''/\partial x) + (1/r)(\partial r v_x''/\partial r))}$, multiplied by r to remove singular behaviour at $r = 0$, and plotted in figure 12. The supersonic case (figure 12*b*) has symmetric pressure diffusion which transports R_{xr} from the edges of the mixing region into the middle of the shear layer. The pressure–strain-rate acts as a sink in the middle of the mixing region and as a small source near the edges. The subsonic case (figure 12*a*) is asymmetric, indicating possible pressure communication across the potential core. In figures 9–11, the cylindrical coordinate redistribution terms were added to the transport terms. These terms are now multiplied by r to make them well behaved at the origin and plotted in figure 13. These redistribution terms in the R_{rr} and $R_{\theta\theta}$ equations are of opposite signs. In any case, the role of all cylindrical redistribution terms are minor. There are also several terms in the transport equations which have not been discussed but are always negligible (see Appendix B).

4.2. *Radially integrated Reynolds stress budgets*

Radially integrated budget quantities are indicated with $\check{(\cdot)}$ and, using dissipation ε as an example, are defined as

$$\check{\varepsilon} = \int_0^\infty \varepsilon r \, \mathrm{d}r. \tag{4.2}$$

When radially integrated, the Reynolds stresses obey the following set of ordinary differential equations in time

$$\partial_t \check{R}_{xx} = \check{\mathscr{P}}_{xx} - \check{\Pi}_{xx} - \check{\varepsilon}_{xx}, \tag{4.3}$$

$$\partial_t \check{R}_{rr} = \check{\Pi}_{rr} - \check{\varepsilon}_{rr}, \tag{4.4}$$

$$\partial_t \check{R}_{xr} = \check{\mathscr{P}}_{xr} - \check{\Pi}_{xr} - \check{\varepsilon}_{xr}. \tag{4.5}$$

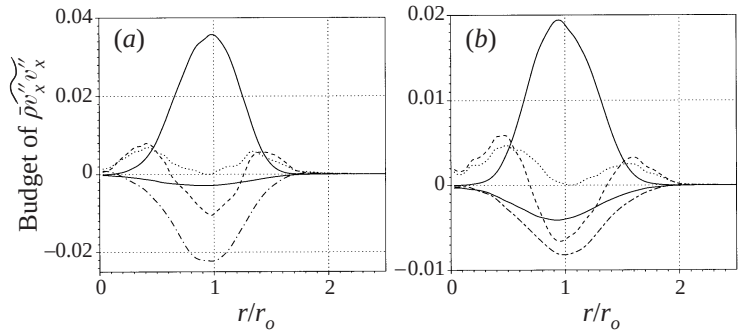

FIGURE 8. $\widetilde{\bar{\rho}v_x''v_x''}$ budget terms normalized by $\rho_j U_j^3/r_o$ at $\delta_m = 0.2r_o$ for (*a*) $M_c = 0.21$ and (*b*) $M_c = 0.99$. ——, Production when positive dissipation when negative; – – –, turbulent transport; —·—, pressure–strain-rate redistribution = pressure–velocity-gradient; ·····, time rate of change.

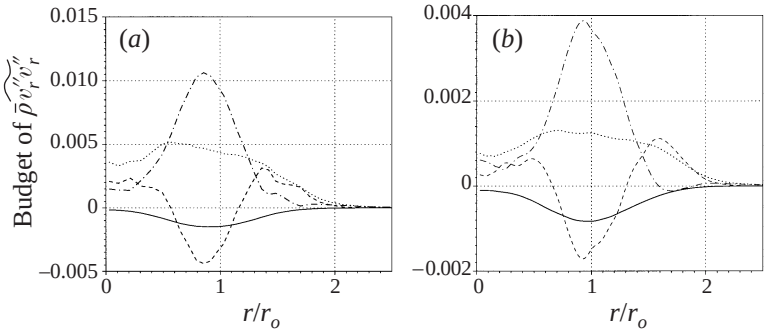

FIGURE 9. $\widetilde{\bar{\rho}v_r''v_r''}$ budget terms at $\delta_m = 0.2r_o$ normalized by $\rho_j U_j^3/r_o$ at $\delta_m = 0.2r_o$ for (*a*) $M_c = 0.21$ and (*b*) $M_c = 0.99$. ——, Viscous dissipation; – – –, turbulent transport + cylindrical redistribution; —·—, velocity–pressure-gradient; ·····, time rate of change.

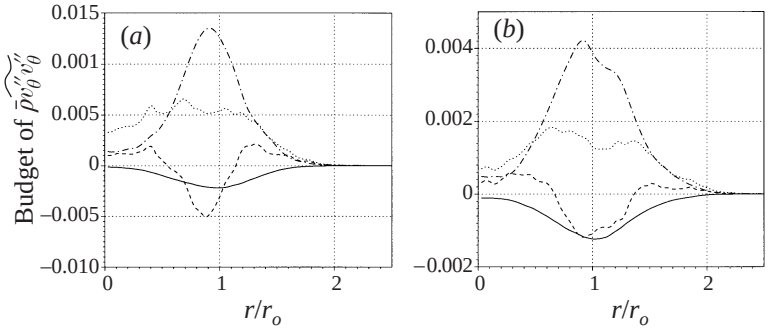

FIGURE 10. $\widetilde{\bar{\rho}v_\theta''v_\theta''}$ budget terms at $\delta_m = 0.2r_o$ normalized by $\rho_j U_j^3/r_o$ at $\delta_m = 0.2r_o$ for (*a*) $M_c = 0.21$ and (*b*) $M_c = 0.99$. ——, Viscous dissipation; – – –, turbulent transport + cylindrical redistribution; —·—, pressure–strain-rate redistribution = velocity–pressure-gradient; ·····, time rate of change.

The shear stress dissipation, ε_{xr}, is negligible compared to the shear stress production ($|\check{\varepsilon}_{xr}| < 0.025\check{\mathscr{P}}_{xr}$ in all cases) and is neglected. All terms are functions of the convective Mach number which is, of course, the parameter of greatest interest in the present study.

These equations, (4.3)–(4.5), were also studied by Vreman *et al.* (1996); but there

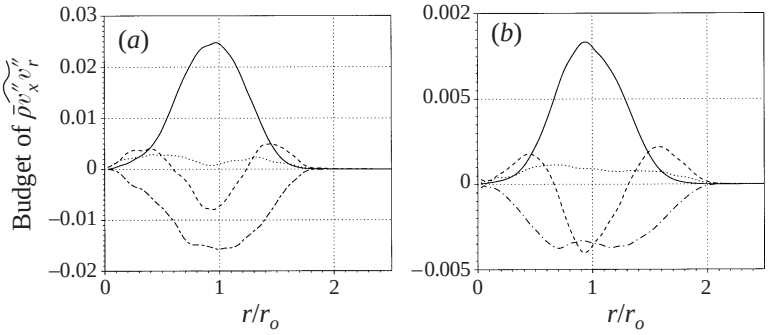

FIGURE 11. $\widetilde{\bar{\rho}v_x''v_r''}$ budget terms at $\delta_m = 0.2r_o$ normalized by $\rho_j U_j^3/r_o$ at $\delta_m = 0.2r_o$ for (*a*) $M_c = 0.21$ and (*b*) $M_c = 0.99$. ——, Production when positive dissipation when negative; – – –, turbulent transport + cylindrical redistribution; —·—, velocity–pressure-gradient; ·····, time rate of change.

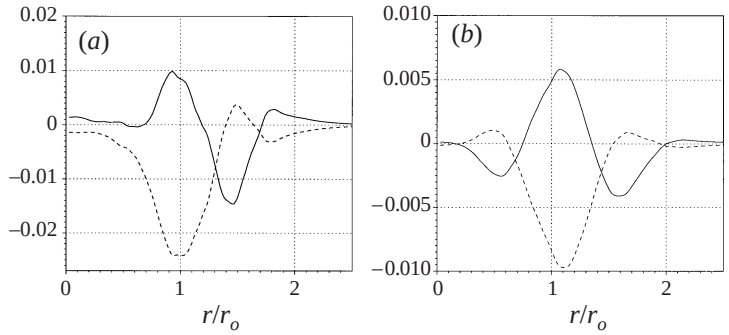

FIGURE 12. – – –, Pressure–strain rate and ——, pressure diffusion terms in the $\widetilde{\bar{\rho}v_x''v_r''}$ transport equation normalized by $\rho_j U_j^3/r_o$ and multiplied by r to remove singular behaviour at $r = 0$. Cases (*a*) $M_c = 0.21$ and (*b*) $M_c = 0.99$.

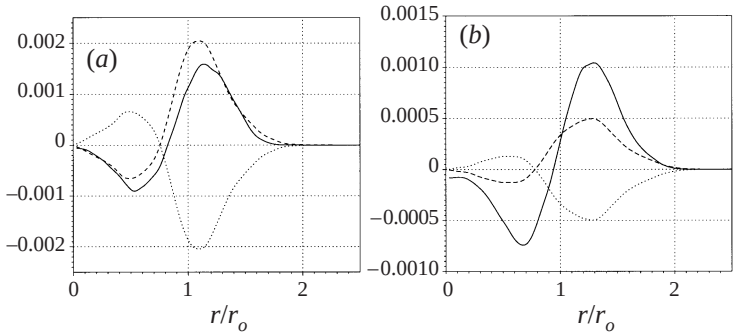

FIGURE 13. Cylindrical coordinate redistribution terms multiplied by r and normalized by $\rho_j U_j^3/r_o$: – – –, $2\overline{\rho v_r'' v_\theta'' v_\theta''}$ from the $\widetilde{\bar{\rho}v_r''v_r''}$ equation; ·····, $2\overline{\rho v_r'' v_\theta'' v_\theta''}$ from the $\widetilde{\bar{\rho}v_\theta''v_\theta''}$ equation; ——, $\overline{\rho v_x'' v_\theta'' v_\theta''}$ from the $\widetilde{\bar{\rho}v_x''v_r''}$ equation. Cases (*a*) $M_c = 0.21$ and (*b*) $M_c = 0.99$.

are significant differences in the analysis (see § 1). In developing a formula for the growth rate, our approach is to observe quantities that are nearly constant with M_c and make appropriate substitutions into the equations.

Referring back to equations (4.3) and (4.4), we see that they are potentially coupled by the pressure–strain-rate Π_{st} which is nearly trace free for all the Mach numbers

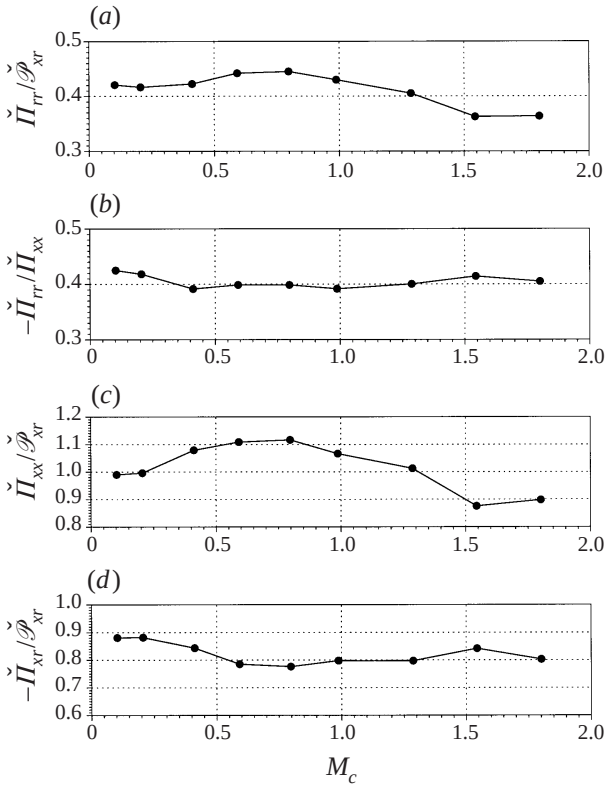

FIGURE 14. Ratios of integrated budget terms.

considered (figure 21) and therefore redistributes R_{xx} to R_{rr} and $R_{\theta\theta}$. Of these, R_{rr} is more important because $\mathscr{P}_{xr} \approx -R_{rr}(\mathrm{d}\bar{u}/\mathrm{d}r)$ and this couples (4.4)–(4.5). We simplify (4.3) to (4.5) by finding ratios that are approximately invariant with Mach number. To start with, we see that both $\check{\Pi}_{rr}/\check{\mathscr{P}}_{xr}$ and $-\check{\Pi}_{rr}/\check{\Pi}_{xx}$ are nearly constant with M_c (figures 14*a*, *b*) and approximately equal to 0.4 which implies that $\check{\Pi}_{xx}/\check{\mathscr{P}}_{xr} \approx 1$ (see figure 14*c*). This indicates that the efficiency of the redistribution of R_{xx} to R_{rr} and the resulting production of R_{xr} is independent of M_c and not responsible for the growth rate suppression. It should also be noted that $-\check{\Pi}_{rr}/\check{\varepsilon}_{rr}$ decreases by 40% with increasing Mach numbers and, thus, changes in $\check{\varepsilon}_{rr}$ are not responsible for the suppression of the turbulence. Similarly, the pressure–strain-rate in the shear stress equation, $\check{\Pi}_{xr}$, is in constant proportion to the shear stress production $\check{\mathscr{P}}_{xr}$ with $\check{\Pi}_{xr}/\check{\mathscr{P}}_{xr} \approx 0.8$ (see figure 14*d*). Also, $\check{\varepsilon}_{xr}/\mathscr{P}_{xr} < 0.025$ in all cases. These observations suggest a simplification of (4.5) to

$$\partial_t \check{R}_{xr} = c_1 \check{\Pi}_{xx}, \tag{4.6}$$

where c_1 is a constant, and results in figures 14(*c*) and 14(*d*) indicate that $c_1 = 0.2$ is a reasonable approximation for all Mach numbers. To derive an expression for δ'_m we may use (2.6) to relate $\check{\mathscr{P}}_{xx}$ to δ'_m (following Vreman *et al.* 1996). Noting that $\check{\varepsilon}_{xx}$ is proportional to $\rho_j U_j^3 r_o$ (figure 15), we replace this ratio with a constant $K_\varepsilon \approx 0.0032$, which reduces (4.3) to

$$\partial_t \check{R}_{xx} = \rho_j U_j^3 r_o(\delta'_m - K_\varepsilon) - \check{\Pi}_{xx}. \tag{4.7}$$

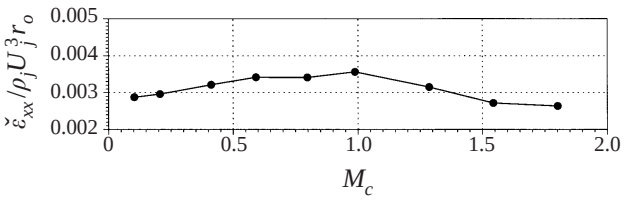

FIGURE 15. Integrated axial normal dissipation with Mach number.

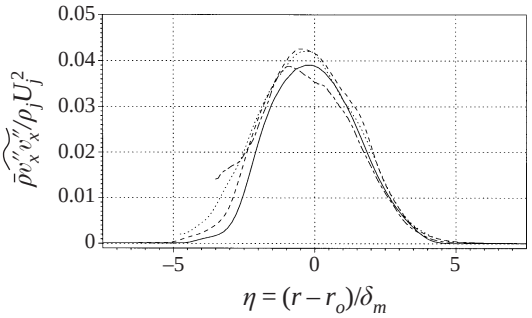

FIGURE 16. Self-similar collapse of axial normal Reynolds stress for the $M_c = 0.99$ case at ——, $tU_j/r_o = 8.1$; – – –, 12.2; ·····, 16.3; — – —, 20.4.

In forming this expression, we have neglected the viscous contribution to the spreading rate in (2.6). This term will later be shown to have only a very small influence.

The time rate of change of the integrated normal stress, $\partial_t \check{R}_{xx}$, may also be related to the growth rate by making a similarity assumption (Vreman *et al.* 1996). The integrated axial normal Reynolds stress is defined as

$$\check{R}_{xx} = \int_0^\infty R_{xx} r \, \mathrm{d}r = \rho_j U_j^2 r_o \delta_m \int_0^\infty \frac{R_{xx}}{\rho_j U_j^2} \frac{r}{r_o} \frac{\mathrm{d}r}{\delta_m}. \tag{4.8}$$

Figure 16 shows profiles of $f(\eta) = R_{xx}/\rho_j U_j^2$ against $\eta = (r - r_o)/\delta_m$ at different times for $M_c = 0.99$ (the $M_c = 0.21$ and other cases are nearly the same). Evidently, the profiles of R_{xx} are nearly self-similar and also largely independent of M_c. This scaling is further supported by figure 17 showing that $a_1 = \check{R}_{xx}/(\rho_j U_j^2 r_o \delta_m) \approx 0.18$ is nearly constant with M_c. However, the flow is not fully self-similar as indicated by the non-zero time rate of change of the turbulence intensities and shear stress in the middle of the mixing layer in figures 8 to 11. Similarly, the mixing layer does not grow linearly in time (figure 32) as would be expected if it were fully self-similar. Nevertheless, the self-similar behaviour of R_{xx} can be used to reduce (4.7) to

$$\delta_m' = \frac{(1/\rho_j U_j^3 r_o)\check{\Pi}_{xx} + K_\varepsilon}{1 - a_1}, \tag{4.9}$$

with $(\partial \delta_m/\partial t) = U_j \delta_m'$.

Equation (4.9) is plotted in figure 18 with $\check{\Pi}_{xx}$ provided by the simulation data, and compared with predictions of the exact equation (2.6). Also plotted is a third curve that corrects (4.9) for the viscous effects. This is obtained by retaining the viscous term in (2.6) where it is used to relate δ_m' to $\check{\mathscr{P}}_{xx}$. The correction is minor and agreement is excellent for both. Also shown in figure 18 is (4.9) applied to the plane mixing-layer simulation data of Vreman *et al.* (1996). Mean values of $\check{\varepsilon}_{11}$ and

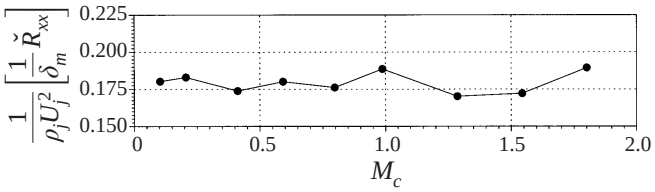

FIGURE 17. Factor relating growth rate and time rate of change of $\bar{\rho}\widetilde{v_x''v_x''}$.

Quantity	Approximate value	Figure
$\check{\Pi}_{rr}/\check{\mathscr{P}}_{xr}$	0.4	14(*a*)
$-\check{\Pi}_{rr}/\check{\Pi}_{xx}$	0.4	14(*b*)
$-\check{\Pi}_{xr}/\check{\mathscr{P}}_{xr}$	0.8	14(*c*)
$K_\varepsilon = \check{\varepsilon}_{xx} r_o/\rho_j U_j^3$	0.003	14(*d*)
$a_1 = \check{R}_{xx}/\rho_j U_j^2 \delta_m$	0.018	17
$\varepsilon_{xr}/\mathscr{P}_{xr}$	< 0.025	—

TABLE 2. Constants determined from database.

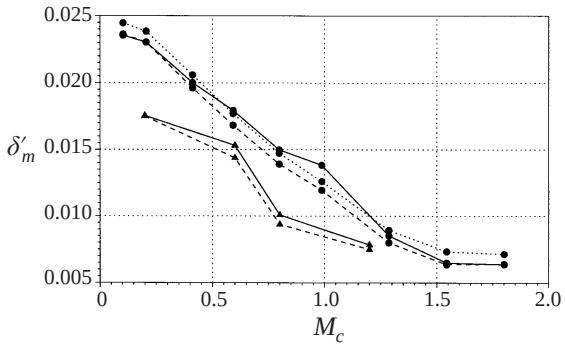

FIGURE 18. Growth rate: ——, measured directly in the simulations; – – –, calculated with (4.9); and ·····, a low-Reynolds-number correction to (4.9) for ●, the present simulations and ▲, the simulation of Vreman *et al.* (1996).

$\check{R}_{11}$ for their cases were used for a_1 and K_ε. Agreement is very good despite (recall R_{xx} is assumed constant in the present analysis) a small suppression of R_{11} in their data and more variation in $\check{\varepsilon}_{11}$ than is observed in the present simulations.

To summarize, the mixing-layer growth rate has been related to a suppression of $\check{\Pi}_{xx}$. It is a sink of $\check{R}_{xx}$ which is nearly constant with Mach number. In the following section we address why $\check{\Pi}_{xx}$ is suppressed. The proportionality and other constants determined from the database are summarized in table 2.

4.3. *Pressure–strain-rate suppression*

Here, we revisit the suppressed pressure fluctuations from § 3.2 and show that their suppressed covariance (relative to $\rho_j U_j^2$) is primarily responsible for the pressure–strain-rate correlation suppression. We will also show that reduced axial fluctuating strain rate makes a small contribution to the suppression of the pressure–strain-rate correlation. Radially integrated r.m.s. pressure fluctuations, pressure–strain-rate, and axial normal strain-rate ($\partial v_x''/\partial x$) are plotted in figure 19. All quantities are normalized

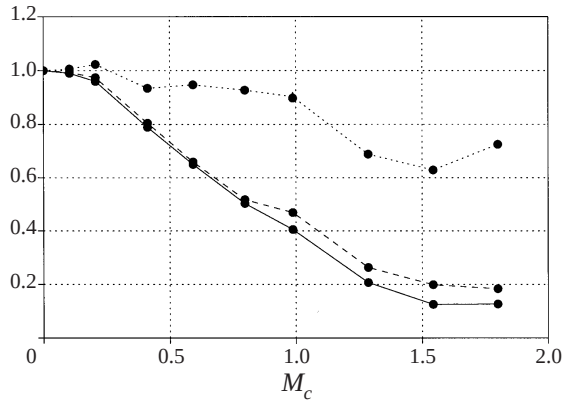

FIGURE 19. Suppression of radially integrated pressure fluctuations, strain rate fluctuations, and pressure–strain-rate correlation from their incompressible values. ——, Π_{xx}; – – –, $p'_{\rm rms}$; ·····, $(\partial u''_x/\partial x)_{\rm rms}$.

by their 'incompressible' values which were estimated with quadratic extrapolation of the $M_c = 0.1$ and $M_c = 0.21$ data. It is clear that the pressure fluctuations are suppressed in the same manner and to nearly the same degree as the pressure–strain-rate correlation which suggests that they are the responsible factor. However, the r.m.s. strain rate is also suppressed to 70% of the incompressible value and this might explain the reduction in Π_{xx} below the pressure fluctuations and pressure–strain-rate at the highest Mach numbers.

Referring back to § 3.3, we see that the scalings suggested there are indeed consistent with the detailed analysis of the turbulence equations presented here. In addition, since it has been shown that it is pressure–strain-rate correlations that regulate the development of the mixing layer and that these in turn scale with ℓ/δ, it is not surprising that the radial and shear components of the Reynolds stress tensor also follow this scaling. Unfortunately, it is difficult to demonstrate this explicitly because of the non-stationarity of this flow. Considering alternative scalings, we expect that since viscous dissipation rates do not appear to explain the gross aspects of the flow development (even in equation (4.4) $\check{\varepsilon}_{rr}$ is roughly proportional to $\check{\Pi}_{rr}$), lengthscales based on ε are inappropriate for scaling the flow. This is elaborated upon in § 6.4. Finally, this analysis has shown why the growth rate does not scale with ℓ/δ, as might be expected given the success of this scaling at collapsing other turbulence statistics (figure 7).

5. Turbulence energetics

5.1. *Transport of turbulent kinetic energy*

Turbulent kinetic energy budgets at $\delta_m = 0.2r_o$ for the $M_c = 0.21$ and $M_c = 0.99$ cases are shown in figure 20. All the terms in the $M_c = 0.21$ case are of similar form to those in the $M_c = 0.99$ case but have roughly twice the magnitude. The dissipation is an exception and has roughly the same magnitude in both. The production in the $M_c = 0.21$ flow is nearly twice that observed by Rogers & Moser (1994) for their unforced incompressible plane mixing layer. However, they report that the levels increased significantly depending upon their initial conditions. Viscous dissipation plays a smaller role relative to the production than was observed by Rogers & Moser (1994), possibly because the small scales in this flow are developing whereas their flow

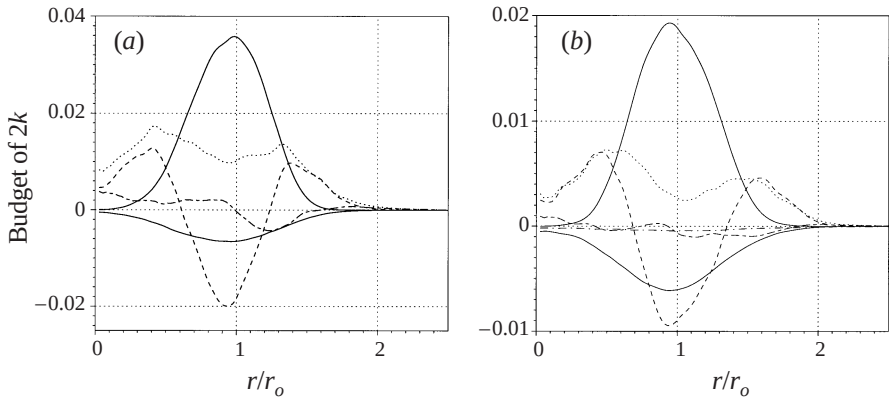

FIGURE 20. $2k = \widetilde{\bar{\rho}v_x''v_x''} + \widetilde{\bar{\rho}v_r''v_r''} + \widetilde{\bar{\rho}v_\theta''v_\theta''}$ budget terms normalized by $\rho_j U_j^3/r_o$ at $\delta_m = 0.2r_o$ for (*a*) $M_c = 0.21$ and (*b*) $M_c = 0.99$. ——, Production when positive, dissipation when negative; – – –, turbulent transport; — – —, velocity–pressure-gradient; — · —, pressure dilatation; ·····, time rate of change.

was self-similar. The spectra in § A.2 show this to be the case. Rogers & Moser (1994) also note relatively less dissipation in their most amplified initial condition case which may better correspond to the present low-Mach-number runs. The velocity–pressure-gradient term does not appear to be statistically converged in the $M_c = 0.99$ case, but is clearly oscillating around zero, indicating that it will have little net influence. The velocity–pressure-gradient in the $M_c = 0.21$ case is smoother and has higher amplitude, but, somewhat surprisingly, is not symmetric about the middle of the mixing region. At $\delta_m = 0.2r_o$, the flow is nearing the point in its development when the potential core begins to close and, after this occurs, all quantities will change from being roughly symmetric about $r = r_o$ to being symmetric about $r = 0$. It is reasonable to expect that terms involving the pressure would be the first to show signs of this transition. It will be shown in § 6.1 that the lower-Mach-number flows have larger and more organized pressure fluctuations and would therefore be more likely candidates for this effect. Regardless, the velocity–pressure-gradient is small compared to the other terms. In the incompressible mixing layer of Rogers & Moser (1994), the velocity–pressure-gradient has a similar amplitude (relative to the production). At both $M_c = 0.21$ and $M_c = 0.99$, the turbulent transport terms are very significant and act to move kinetic energy away from the region of highest shear to the edges of the mixing region.

To examine the direct effect of dilatation upon the energetics we examine the dilatational dissipation (Blaisdell *et al.* 1993) which is defined as

$$\varepsilon_d = \overline{\left(\mu_B + \tfrac{4}{3}\mu\right)\Theta'\Theta'}, \tag{5.1}$$

where $\Theta' = \Theta - \bar{\Theta}$ is the fluctuating dilatation. The solenoidal or incompressible dissipation, ε_s, is the total dissipation minus the dilatational dissipation, $\varepsilon_s = \varepsilon - \varepsilon_d$. The ratio of the radially integrated dilatational to the solenoidal dissipation is plotted in figure 21(*a*) for all the cases. It is clear that even at the highest Mach number, after the growth rate appears saturated, the compressible dissipation is less that 2% of the incompressible dissipation, and we may therefore conclude that it is not responsible for the observed factor of 4 growth rate suppression. The pressure dilatation term is also small, relative to the production (figure 21*b*).

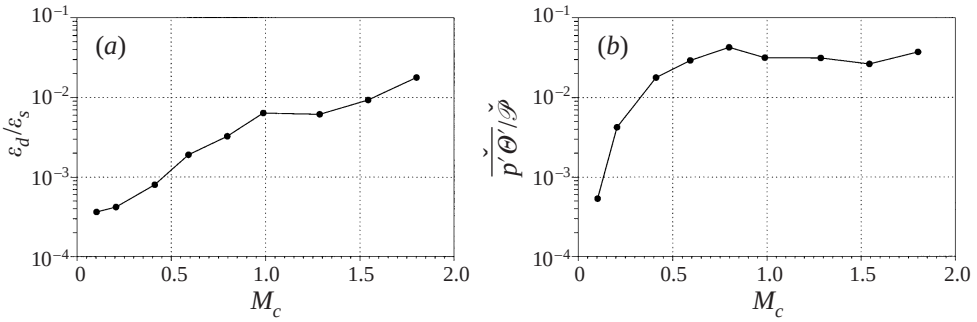

FIGURE 21. (*a*) Ratio of dilatational to solenoidal dissipation and (*b*) ratio of integrated pressure dilatation to the integrated production.

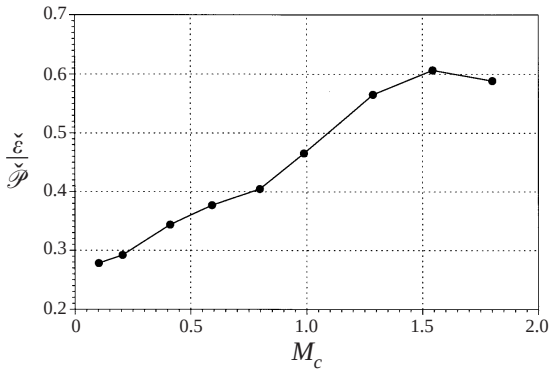

FIGURE 22. Ratio of the integrated dissipation to production for all cases.

Despite minimal dilatational effects, the ratio of the integrated total viscous dissipation to integrated turbulence production increases by a factor of two between the lowest- and highest-Mach-number cases (figure 22). Decreasing production, which drops by a factor of 3.9 between the $M_c = 0.2$ and the $M_c = 1.80$ cases, is primarily responsible for this increase. Sarkar (1995) found a significant decrease in production with increasing Mach number in homogeneous shear flow, as did Vreman *et al.* (1996) in plane mixing layers. This is not surprising because the production of turbulent kinetic energy is related to the momentum thickness growth rate by (2.6). Therefore, reduced $\mathscr{P} \approx \mathscr{P}_{xx}$ and reduced growth rate have a relationship that is closer to an identity than an explanation. In the Reynolds-stress transport equations, $\mathscr{P}_{xx}$ is a source of R_{xx}, but, clearly, R_{xr} acts to spread the layer:

$$\frac{\partial \bar{\rho}\tilde{v}_x}{\partial t} + \frac{1}{r}\frac{\partial \bar{\rho} r \tilde{v}_x \tilde{v}_r}{\partial r} = -\frac{1}{r}\frac{\partial r \bar{\rho}\widetilde{v_x'' v_r''}}{\partial r} + \frac{1}{r}\frac{\partial r \bar{\tau}_{xr}}{\partial r}. \tag{5.2}$$

Since R_{xx}, when normalized by $\rho_j U_j^2$, is independent of M_c (figure 3), the decrease in $\mathscr{P}_{xx}$ at high Mach numbers does not provide a satisfactory explanation for the level of R_{xr} and thereby the growth rate. Thus, energetics alone do not seem sufficient to explain the suppressed growth. It is the mechanism discussed in 4.2 by which the energy is removed from R_{xx} and produces R_{xr} that regulates growth rate. Therefore, models based on turbulent kinetic energy (e.g. a k–ε model) to predict shear-layer compressibility effects are physically unrealistic.

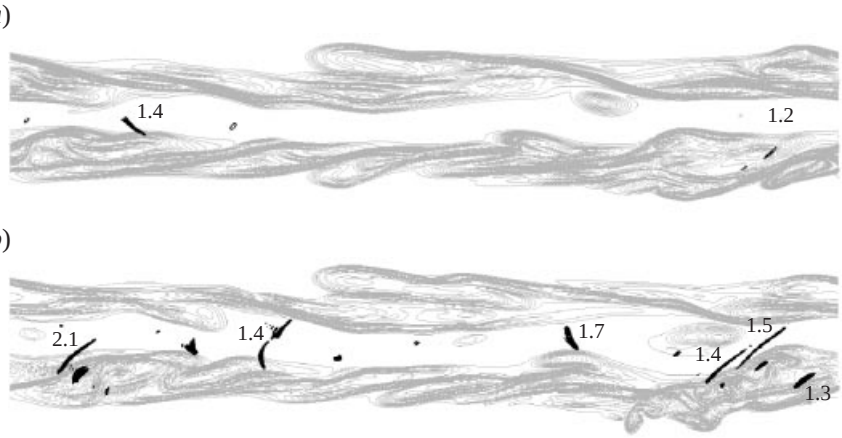

FIGURE 23. Grey: contours of vorticity magnitude. Black: regions of negative dilatation $\Theta < 0.67U_j/r_o$. (*a*) $M_c = 1.54$; (*b*) $M_c = 1.80$ at $\delta_m = 0.2r_o$.

5.2. *Shocklets*

Small shocks associated with turbulent eddies, which have come to be known as 'eddy shocklets', were first observed in two-dimensional isotropic turbulence simulations of Passot & Pouquet (1987). Subsequently, they have been observed and studied in three-dimensional decaying isotropic turbulence (Lee, Lele & Moin 1991), two-dimensional mixing layers (Lele 1989; Sandham & Yee 1989), and three-dimensional mixing layers (Vreman *et al.* 1996). Experimental evidence of shocklets has also been reported in a counterflowing supersonic shear layer (Papamoschou 1995).

It is difficult to define what a shocklet is. We will use regions of strong negative dilatation to mark what will be referred to as shocklets in the present discussion. These regions are shown in figure 23 for the $M_c = 1.54$ and 1.80 cases at the $\delta_m = 0.2r_o$ point. Light contours of vorticity magnitude are also shown to place the positions of the shocklets relative to the turbulent shear layer. The dilatation is not large relative to the vorticity magnitude; the peak negative dilatation is a factor of 4 smaller than the peak vorticity magnitude. It is clear that some of the shocks are in irrotational regions and it is a matter of definition whether they are eddy shocklets or another type of shock such as weak oblique shocks. The numbers adjacent to the shocklets in figure 23 indicate pressure ratios, p_1/p_2, across the shock. Estimates of normal Mach numbers were within roughly 30% of steady shock jump conditions. Direct comparison was difficult for three reasons: these weak low-Reynolds-number shocks have a finite width which is difficult to measure consistently; the flow near the shocks, particularly the stronger shocks, is locally poorly resolved; and the shocks are not steady and therefore tabulated shock jump conditions for steady flow do not strictly apply. The shocks occupy a small volume fraction of the flows considered and the local under-resolution, which manifests itself in artificially increased high-wavenumber energy (figure 36), is not believed to affect the overall turbulence dynamics.

The convective Mach number, at which shocklets have been observed to form, depends on whether the flow is two- or three-dimensional. Shocks were observed in two-dimensional shear flows at convective Mach numbers as low as $M_c = 0.7$ (Lele 1989; Sandham & Yee 1989) but not until the convective Mach number reaches $M_c = 1.2$ in three-dimensional flows (Vreman *et al.* 1995, 1996). In the present

simulations, the first shocklets are observed at $M_c = 1.54$ which is at a higher Mach number than the previous three-dimensional simulations. There are several possible explanations for this. It may be due, in part, to the lack of a definitive criterion of when a pressure disturbance is not a strong acoustic wave but a shock. The definition used by Vreman *et al.* (1995) was a diagnostic condition to designate the method of finite differencing and was therefore dependent upon the grid spacing and not universally applicable. However, we did not observe a factor of 2 pressure jump until $M_c = 1.8$, but jumps of this size were observed in simulations of Vreman *et al.* at $M_c = 1.2$. The annular flow geometry is certainly another difference with their plane mixing layer, but there is nothing to suggest that shocks would be less likely to form in the annular mixing region. Yet another possibility is the influence of initial conditions. The initial conditions of the present simulations are different from those of Vreman *et al.* and perhaps the instability waves used as initial conditions in that study gave rise to structures which are more coherent and may have higher pressure field influences. A final possibility is that their flow remains correlated in space. It is reasonable that a spatially correlated simulation may exhibit shocklets at a Mach number somewhere between a fully decorrelated three-dimensional flow and two-dimensional flow. Vreman *et al.* (1995, 1996) do not document the adequacy of the extent of their computational box, and two-point correlations from their simulations may not have decayed sufficiently to justify the use of periodic boundary conditions in the homogeneous directions.

5.3. *Morkovin's hypothesis*

Morkovin's hypothesis relates temperature, density, and velocity fluctuations in compressible turbulent boundary layers and is useful, when applicable, for modelling compressible turbulence. Morkovin (1961) assumed that pressure fluctuations in adiabatic wall compressible boundary layers are negligible compared to vorticity and entropy fluctuations and that total temperature fluctuations are negligible. When combined, these assumptions,

$$\frac{p'}{\bar{p}} \ll \frac{\rho'}{\bar{\rho}}, \quad \frac{T_o'}{\bar{T}_o} \ll 1, \tag{5.3}$$

lead to a relation between the density, temperature and streamwise velocity fluctuations

$$\frac{\rho'}{\bar{\rho}} \approx -\frac{T'}{\bar{T}} \approx (\gamma - 1)M^2 \frac{u'}{\bar{u}}. \tag{5.4}$$

The hypothesis has been tested in compressible boundary layers and holds for $M_\infty < 5.0$ (Bradshaw 1977).

The application of the hypothesis to compressible free shear flows is less clear. Bradshaw (1977), pointing to the incompressible mixing-layer results of Brown & Roshko (1974), claims that suppression of growth rate is a real compressibility effect associated with a breakdown of Morkovin's hypothesis. He concludes that since the density fluctuations are not responsible for the suppressed mixing-layer growth, increased pressure fluctuations must then be responsible.

The present flow has nearly uniform temperature, and so, at higher Mach numbers, the stagnation temperature, T_o, has significant fluctuations (at fixed Eulerian position). So we will not test the portion of the hypothesis based on this assumption. However, we may test the $p'/\bar{p} \ll \rho'/\bar{\rho}$ assumption. In figure 24, radially integrated root-mean-squared perturbations are plotted. At low Mach numbers, the pressure fluctuations are clearly subordinate to the temperature and density fluctuations. However, after

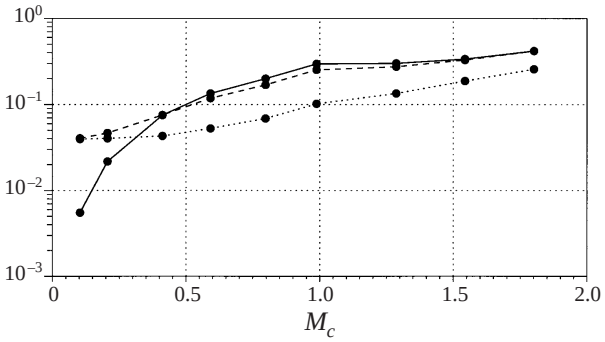

FIGURE 24. Radially integrated root-mean-squared thermodynamic fluctuations normalized by their mean values: ——, $p'_{\rm rms}/\bar{p}$; – – –, $\rho'_{\rm rms}/\bar{\rho}$; ·····, $T'_{\rm rms}/\bar{T}$.

$M_c \approx 0.4$, they have nearly the same amplitude, relative to their mean values, as the density fluctuations. The root-mean-squared temperature fluctuations are less significant relative to their mean than either the pressure or density fluctuations. In related work it was found that the thermodynamic fluctuations were approximately isentropically related for $M_c \lessapprox 1.3$ (Freund *et al.* 1997).

It is clear that the assumption of negligible pressure fluctuations is not well founded for the present flow. Of course, if the temperature ratio across the layer were larger, the low Mach number temperature and density fluctuations would also be larger and the condition $p'/\bar{p} \ll \rho'/\bar{\rho}$ may hold over a wider range of Mach numbers. The assumption of negligible pressure fluctuations appears flawed nonetheless.

The breakdown of the hypothesis, via increasing pressure fluctuations relative to density and temperature fluctuations, has serious implications for the use of hot wires in transonic turbulent flows where the assumption $p'/\bar{p} \ll \rho'/\bar{\rho}$ or $T'/\bar{T}$ is used (see recent work of Barre, Quine & Dussauge (1994) and the references listed therein). In addition, the extension of incompressible Reynolds-averaged Navier–Stokes models to compressible flows is often justified using Morkovin's hypothesis (for a review see Knight 1997).

6. Implications and discussion

6.1. *Large-eddy structural changes*

The significant decrease in radial lengthscale has definite implications for the large turbulent structures in the flow. Though no rigorous connection is available, regions of low pressure are typically associated with large vortical structures and are therefore used here to visualize the flow. Pressure iso-surfaces, at a single pressure level (normalized by $\rho_j U_j^2$), for the $M_c = 0.21$, 0.59, 0.99, and 1.29 cases reveal a dramatic change in the large-scale structures with increasing Mach number (figure 25). This particular iso-level was chosen to accent the large structures in the $M_c = 0.21$ flow, and the effect of changing it is discussed below. The $M_c = 0.21$ flow (figure 25*a*) is dominated by large roller structures which are connected by finer rib-type structures (Moser & Rogers 1993; Clemens & Mungal 1995). The regions of low pressure radially span the mixing region. At $M_c = 0.59$ (figure 25*b*), the large rollers are less prevalent and the streamwise vortices are pronounced. This is consistent with linear stability analysis for plane mixing layers (Sandham & Reynolds 1990) which shows that oblique modes become more unstable with increasing convective Mach number. Experiments also

show increasing three-dimensionality with increasing Mach number (Papamoschou & Roshko 1988; Fourguette *et al.* 1991; Göebel & Dutton 1991; Clemens & Mungal 1995; Samimy, Reeder & Elliott 1992). This observation was also made in previous simulations into early nonlinear regimes (Sandham & Reynolds 1991). At $M_c = 0.99$ (figure 25*c*) there is no evidence of Kelvin–Helmholtz rollers. Instead, the iso-surfaces indicate that the flow is dominated by streamwise oriented vortices. It is also clear that a much smaller fraction of the flow volume is below the normalized threshold pressure. This trend continues to $M_c = 1.29$ (figure 25*d*) where almost none of the flow is now below the threshold pressure and the portion which is, is oriented in the streamwise direction. The highest-Mach-number flows (not shown) continue this trend still further, but so little of the flow is below the threshold pressure that they are not plotted.

It is conceivable that the low-Mach-number structures in figure 25(*a*) might become visible at pressure iso-levels closer to p_∞ for high-Mach-number flows. This possibility is explored in figure 26 where different pressure iso-levels are plotted for the $M_c = 1.29$ flow. It is clear that the large low-Mach-number structures do not reappear. Plotting iso-levels closer to p_∞ than that shown in figure 26(*b*) is difficult because pressure fluctuations associated with the acoustic near-field, which is quite intense in the high-Mach-number flows, obscure the turbulent region.

6.2. *Lengthscale implications for structure convection velocities*

The significant decrease in transverse turbulence lengthscale has interesting implications for measurements of large-structure convection velocities in compressible mixing layers (Dimotakis 1991; Fourguette *et al.* 1991; Messersmith & Dutton 1996; Papamoschou 1997). Since the transverse extent of these structures is suppressed by over a factor of 2, it is unlikely that the well-known derivation of M_c based on isentropic stagnation point arguments (Papamoschou & Roshko 1988) is at all realistic at higher Mach numbers. Assuming that in the incompressible limit the structures, at most, span the mixing layer, then the dynamically important structures at high Mach number do not extend across the mixing layer. Observations that are made based on scalar fields in which large structures appear to span supersonic mixing layers ave therefore misleading and it is likely that these apparent δ-scale structures are not dynamically significant in a statistical sense. One possible explanation for their appearance is that they are remnants of earlier, dynamically significant structures whose velocity perturbations have decayed but for which the scalar field remains distorted. If they do not span the mixing layer, it is not surprising that structures appear to convect at speeds nearer to one of the free-stream velocities than the so-called isentropic convection velocity (Dimotakis 1991; Papamoschou 1997). As a result, mixing models which rely on δ-scale structures (Broadwell & Breidenthal 1982; Dimotakis 1989) may require adjustment at higher Mach numbers.

6.3. *Timescale analysis*

It still remains unclear what causes the change in structure reflected in the visualization in § 6.1 and in the reduced transverse lengthscales calculated in § 3. We may examine possible causes by considering the different timescales of the flow. These are nicely summarized by Simone *et al.* (1997). Adapting their list to the present coordinates and notation, they are a mean flow distortion timescale

$$\tau_d^{-1} = \frac{\partial \bar{v}_x}{\partial r} \equiv S, \tag{6.1}$$

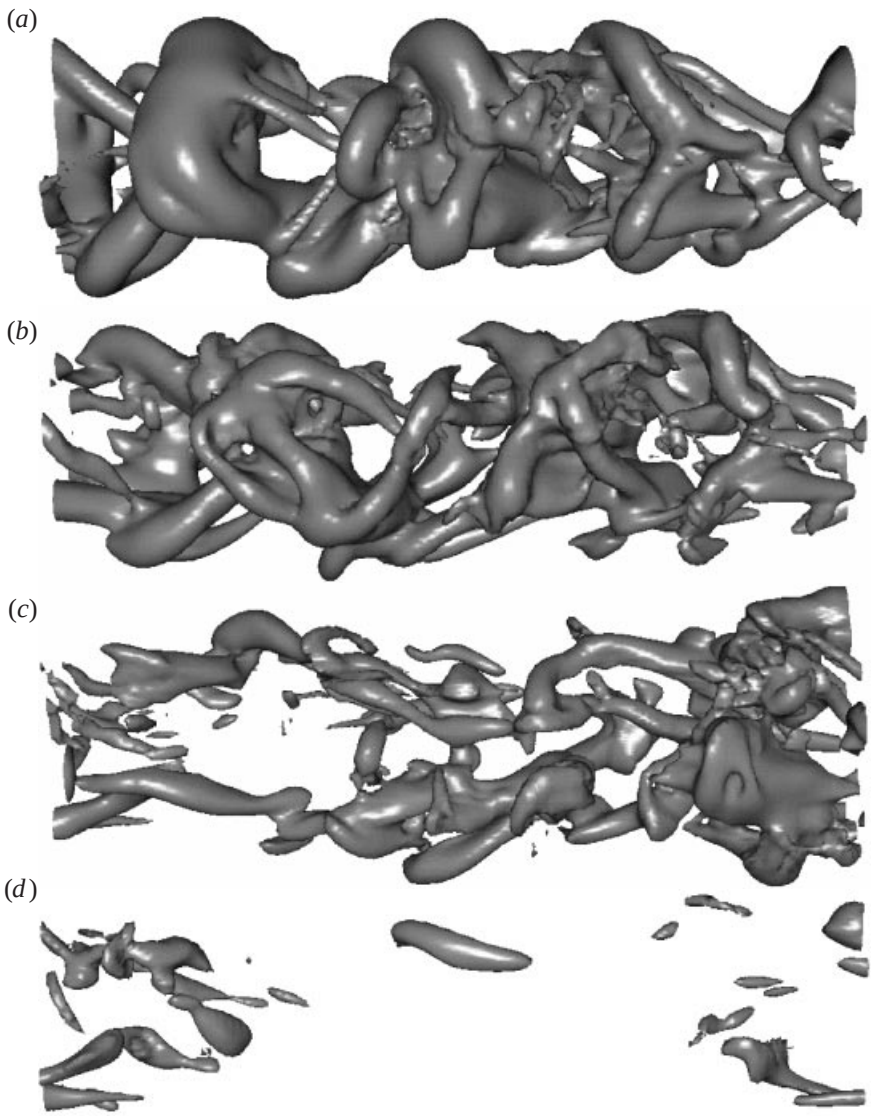

FIGURE 25. Pressure iso-surfaces for the (*a*) $M_c = 0.21$, (*b*) $M_c = 0.59$, (*c*) $M_c = 0.99$, and (*d*) $M_c = 1.29$ at the $\delta_m = 0.2r_o$ point. Only half the axial domain is shown. The pressure level in all cases is $(p_{\rm iso} - p_\infty) = -0.027\rho_\infty U_j^2$.

a turbulence timescale (a large-eddy turn-over time)

$$\tau_t^{-1} = (\overline{v_r' v_r'})^{1/2}/\ell, \tag{6.2}$$

and an eddy-acoustic timescale based on the large-eddy lengthscale and the sound speed

$$\tau_a^{-1} = \bar{a}/\ell. \tag{6.3}$$

Transverse lengthscales and velocities are used because these are the most important for spreading the mixing layer. In computing values, all quantities are taken from the middle of the mixing layer. We next consider ratios of these timescales as potential

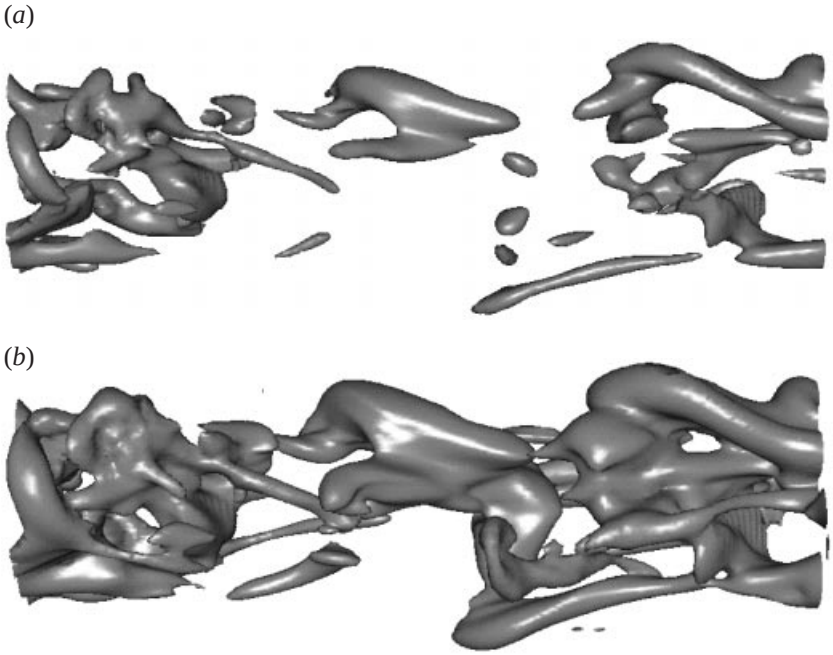

FIGURE 26. Pressure iso-surfaces for the $M_c = 1.29$ flow at the $\delta_m = 0.2r_o$ point. Only half the axial domain is shown. The pressure levels, $(p_{\rm iso} - p_\infty)/\rho_\infty U_j^2$, are (*a*) −0.018, (*b*) −0.010.

parameters. Unfortunately, in contrast to homogeneous model flows, it is difficult or impossible to independently vary the timescales to study their effects individually.

6.3.1. *Rapid distortion effects* – τ_t/τ_d

The ratio τ_t/τ_d is often used in incompressible turbulence to quantify the degree to which rapid-distortion effects govern the flow. It has been shown that many phenomena observed in the present study have counterparts in rapid-distortion (RDT) models of compressible homogeneous shear flow (Simone *et al.* 1997). Related to this, and since τ_t/τ_d is potentially an important parameter in the present flow, one may ask whether or not rapid-distortion effects might increase as the Mach number increases and thereby explain some of the changes with increasing Mach number. To examine this, τ_t/τ_d is plotted in figure 27. Also shown is the more traditional RDT parameter Sq^2/ε, where $q^2 = (\overline{v_x'v_x'} + \overline{v_r'v_r'} + \overline{v_\theta'v_\theta'})$. In the latter case q^2/ε takes the place of the turbulence timescale, but given the poor performance of q^3/ε as a relevant lengthscale in this developing flow (see § 6.4), it is a less reliable estimate. It is clear in figure 27 that RDT effects should not increase significantly with Mach number. This does not mean that linearized analysis cannot potentially explain the observed effects (Simone *et al.* 1997), but only that RDT effects are not increasing with M_c for this flow.

6.3.2. *Turbulence Mach number* – τ_a/τ_t

The ratio of the eddy-acoustic timescale to the turbulence timescale gives a transverse turbulence Mach number, $M_{t_r} = \tau_a/\tau_t$, which is potentially an important parameter. This quantity increases with M_c at low Mach numbers and then appears to level off for $M_c > 1$ (figure 28). $M_t = q/\bar{a}$, also plotted in figure 28, does not level off. This behaviour indicates that the compressibility of the important transverse velocity

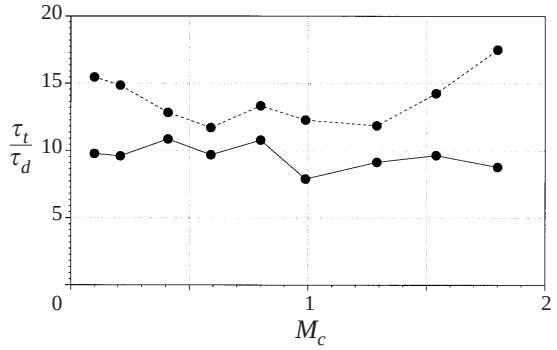

FIGURE 27. Ratio of turbulent to mean-distortion timescale at $r = r_o$: ——, $\tau_t/\tau_d = S\ell/(\overline{v_r'v_r'})^{1/2}$; – – –, $\tau_t/\tau_d = Sq^2/\varepsilon$.

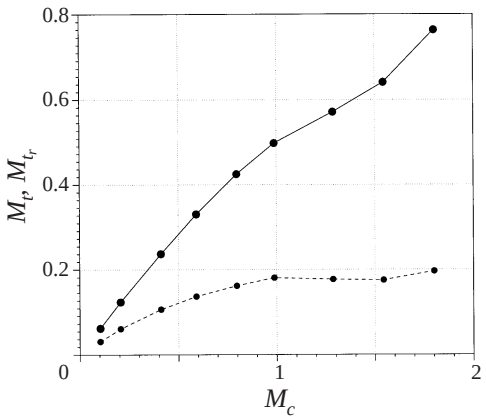

FIGURE 28. Turbulence and transverse turbulence Mach numbers at $r = r_o$: ——, M_t; – – –, M_{t_r} (see text).

fluctuations saturates while the standard measure of turbulence compressibility, M_t, deceptively continues to increase.

6.3.3. *Gradient Mach number* – τ_a/τ_d

The final timescale ratio, which is often called the gradient Mach number $M_g = \tau_a/\tau_d = S\ell/\bar{a}$, has recently been shown to be an important parameter by Sarkar (1995) in homogeneously sheared turbulence and by Simone *et al.* (1997) in rapid-distortion analysis of compressible turbulent homogeneous shear flow (there it was called the 'distortion Mach number', M_d). The gradient Mach number calculated at $r = r_o$ grows quickly at first before it appears to asymptote to a value around 2 (figure 29). This behaviour disagrees with the estimate made by Sarkar (1995) that $M_g = 2.2M_c$ because his estimate used an incompressible mixing-layer lengthscale, $\ell = \delta$, and did not account for the large decrease of ℓ shown in figure 6. However, this behaviour does not invalidate his conclusions concerning the role that the gradient Mach number plays in describing the very different compressibility effects in mixing layers and boundary layers. The gradient Mach number for the present mixing layer is still many times larger than his estimate for boundary layers. It should also be noted that up to $M_c \approx 0.75$, Sarkar's estimate is quite good.

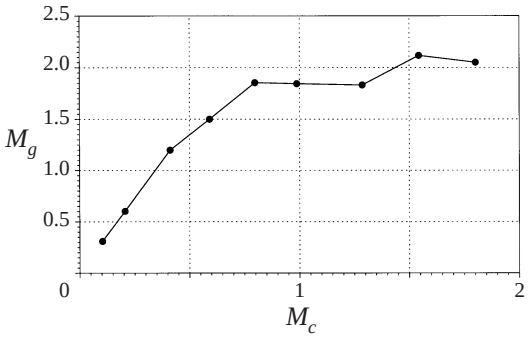

FIGURE 29. Gradient Mach number at $r = r_o$.

6.3.4. *A heuristic interpretation of M_g*

The timescales discussed above offer an explanation for why ℓ decreases with increasing Mach number. If τ_d is significantly shorter than τ_a, the large eddies are being deformed more rapidly than sound can propagate across them. Since the sound speed plus flow velocity locally sets the peak speed for 'information' to propagate, it is impossible for eddies having $\tau_a > \tau_d$ (with appropriate constants assumed) to remain coherent. This restricts ℓ. Some studies have considered separate incompressible and compressible contributions to the pressure (e.g. Sarkar 1995), which would allow large eddies to remain coherent since a Poisson equation is solved for the incompressible portion of the pressure, but this is purely a kinematic decomposition. This 'communication'-limited dynamics of large structures across the mixing layer, which is inherent in the deterministic model of Vreman *et al.* (1996) and the sonic eddy concept of Breidenthal (1990), suggests that the gradient Mach number should saturate with increasing M_c, a trend observed in the simulation data.

This reasoning is also in line with a discussion presented by Lighthill (1955) who pointed out that in a compressible turbulent flow the required incompressible 'readjustment of pressure has changed by the time the signal arrives'. He used this to explain aspects of sound generation and compressible turbulence, and also proposed a mechanism based on pressure fluctuations for the suppression of turbulence in jets with increasing Mach numbers which was dependent upon dissipation of acoustic waves. As seen in § 5.1, we do not observe a significant dynamic role played by the increase in the dissipation. It was also verified that the sum of all energy budget terms was nearly zero, which indicates that the radiated acoustic energy was negligible.

6.3.5. *Pressure-variance scaling revisited*

The pressure variance is seen (figure 30) to scale well as either

$$\overline{p'p'} = K_g \bar{\rho}^2 \left(\frac{\partial \bar{v}_x}{\partial r} \right)^4 \ell^4 \propto M_g^4, \tag{6.4}$$

or

$$\overline{p'p'} = K_{t_r} \bar{\rho}^2 (\overline{v_r' v_r'})^2 \propto M_{t_r}^4, \tag{6.5}$$

where K_g and K_{t_r} are proportionality constants set to match the simulation data at $M_c = 0.2$. Also shown for reference in figure 30 is $\overline{p'p'} = K_u \bar{\rho}^2 U_j^4$ with K_u also set to match the data at $M_c = 0.2$. Evidently, the suppressed pressure fluctuations can be interpreted as either due to saturation of v_r' owing to compressibility (parameterized by M_{t_r}), or due to eddy-acoustic timescale limitation parameterized by M_g. However,

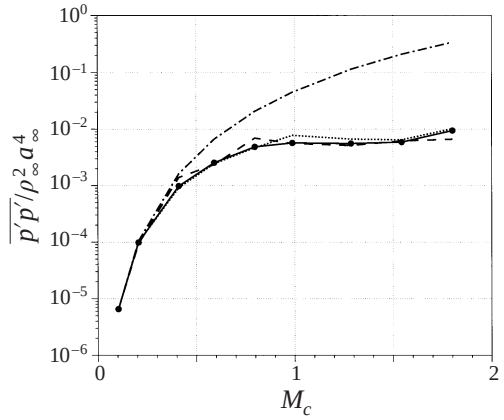

FIGURE 30. 'Un-normalized' pressure fluctuations at $r = r_o$: ——, from the simulations; – – –, $\sim M_g^4$ from (6.4); ·····, $\sim M_{tr}^4$ from (6.5); —·—, $\sim U_j^4$ (see text).

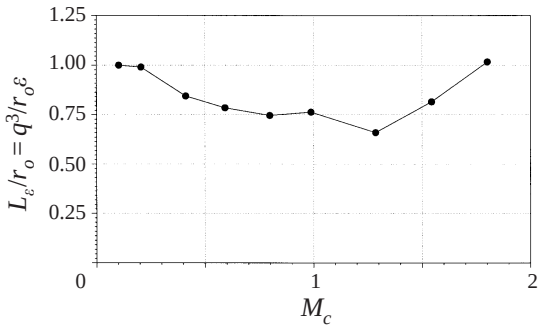

FIGURE 31. Turbulence lengthscale at $r = r_o$.

both of these interpretations relate to the fluid compression only indirectly. The quintessential element appears to be the decreased transverse lengthscale of the turbulence.

6.4. *Criticism of alternative lengthscales*

Bradshaw (1996) criticizes the gradient Mach number as a parameter to account for compressibility effects. He assumed that $\ell = q^3/\varepsilon$, as is often done in modelling, and rewrote the gradient Mach number as $M_g = M_t(Sq^2/\varepsilon)$. Proceeding further, he assumed that $b_{12} = \overline{u'v'}/q^2$ was nearly constant to arrive at $M_g \propto M_t\mathscr{P}/\varepsilon$ which is attractive because it leaves the compressibility in a single parameter, M_t. However, these choices are not supported by the present simulations. In figure 4 it is shown that b_{12} changes by over a factor of 2 for the range of Mach numbers studied. In addition, $L_\varepsilon = q^3/\varepsilon$ behaves differently from ℓ. Shown in figure 31, it falls by 25% at intermediate Mach numbers before increasing for the highest M_c cases. Evidently, L_ε does not contain the physical information contained in the transverse correlation scale ℓ.

7. Conclusions

Direct numerical simulation was used to study turbulence in an annular compressible free shear flow. To isolate compressibility effects, the Mach number was

varied from low subsonic ($M_j = 0.2, M_c = 0.1$) to supersonic ($M_j = 3.5, M_c = 1.8$) while other flow parameters were fixed. The turbulence at all Mach numbers was shown to be decorrelated within the computational box, and energy spectra indicated that it was realistically broadbanded. The growth of the mixing layer and the Reynolds stresses were suppressed with increasing Mach number, similar to experiments. A new velocity scaling based upon the mean velocity difference across a typical large eddy was proposed and shown to collapse the data.

Terms in the Reynolds-stress transport equations were examined in detail and these equations were simplified based on the statistics from the databases. This led to a simple formula that related the growth rate to the pressure–strain-rate correlation term in the $\bar{\rho}\widetilde{v_x''v_x''}$ equation. Examination of pressure and strain-rate fluctuations independently showed that the behaviour of this correlation was due, for the most part, to suppressed pressure fluctuations, though strain-rate suppression also played a minor role. It is concluded that any attempts to model compressible Reynolds-stress closures for compressible turbulence must pay particular attention to modelling the pressure–strain-rate correlation.

Dilatational effects were found to have negligible direct influence upon the turbulence energetics. This was the case despite the fact that weak shocklets were found in the highest-Mach-number flows. The shocks first appeared at $M_c = 1.54$, which was higher than in previous studies.

Flow visualization showed dramatic structural changes as a function of Mach number. Pressure iso-surfaces showed that the flow at low Mach number was dominated by large azimuthally correlated structures whereas at higher Mach numbers these large structures were no longer apparent. Instead, smaller streamwise oriented structures were prevalent at high Mach numbers.

An analysis of timescales showed that the pressure fluctuations, and hence the growth rate suppression, could be parameterized with either a transverse turbulence Mach number or the gradient Mach number, though no direct link to true compressibility in the form of a finite divergence of the fluctuating velocity field was discovered. The timescale analysis also showed that RDT effects did not increase with increasing M_c. A heuristic interpretation of M_g provided a possible explanation for the decrease of the transverse lengthscale based on relative timescales. The decrease in this lengthscale appears to be the principal factor affecting the observed gross behaviour of the flow.

J. B. F. acknowledges the support of the Caroline M. and Franklin P. Johnson graduate fellowship at Stanford University. Computer time was provided by CEWES, ASC, MHPCC, NAS, and ARC.

Appendix A. Flow development and fundamental documentation of the database

The purpose of this appendix is to document the development of the flow up to, and in some instances beyond, the $\delta_m = 0.2r_o$ point studied in the body of the paper. At the same time, it also serves to emphasize the realism of the computed flow by showing broadbanded turbulence spectra and two-point correlations that realistically decay to small values within the computational box.

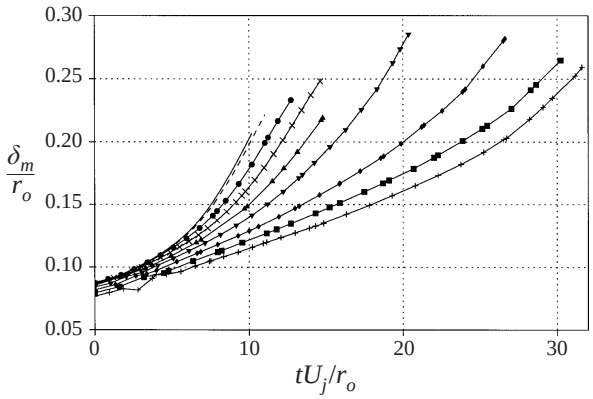

FIGURE 32. Momentum thickness as the flow develops for ——, $M_c = 0.10$; – – –, $M_c = 0.21$; ●, 0.41; ×, 0.59; ▲, 0.79; ▼, 0.99; ◆, 1.29; ■, 1.54; +, 1.80.

A.1. *Mean flow*

A.1.1. *Mixing layer thickness and growth*

A plot of momentum thickness against normalized time for a single realization of all the cases shows that the higher-Mach-number mixing layers grow more slowly (figure 32). As discussed in § 2.4, the present flow is not self-similar and so the growth rate varies in time. It is clear from figure 32 that comparing the $M_c = 0.10$ and the $M_c = 1.80$ growth rates at the same non-dimensional time would be making a comparisons of flows at very different points in their development, hence the choice of a thickness, $\delta_m = 0.2r_o$, in the body of the paper for the point at which to compare data.

A.1.2. *Similarity of axial velocity profiles*

Typically, in spatially developing plane mixing-layer studies the flow is either assumed or demonstrated to be self-similar and a similarity variable, such as $\eta = y/\delta(x)$, is used to collapse the data from different downstream locations. The temporally developing case may be approached in an analogous manner. To quantify the present mean axial velocity evolution in this context and establish an avenue for more general application of the results, we attempt to collapse the mean velocity of the $M_c = 0.21$ and $M_c = 0.99$ cases using $\eta = (r - r_o)/\delta_m$ (figure 33). Considering the multiple lengthscales of the flow, the data collapses well up to the point when the potential core closes. The axial velocity profiles of the other cases may be similarly collapsed. Comparing the axial velocity profiles from the different simulations in this manner does not yield any trends with increasing Mach number. Similar insensitivity has been observed experimentally (Samimy & Elliott 1990).

A.1.3. *Mean temperature*

The mean temperature in the mixing region is a function of the Mach number owing to viscous dissipative heating which is significant in the highest-Mach-number cases. The initial temperature profiles, specified by the Crocco–Busemann relation, and the temperature profiles when the momentum thickness is $\delta_m = 0.2r_o$ are plotted in figure 34. The $M_c = 0.10$ and $M_c = 0.21$ cases are indistinguishable. It was found that the temperature at $\delta_m = 0.2r_o$ obeys a turbulent analogue to the Crocco–Busemann relation (Freund *et al.* 1997).

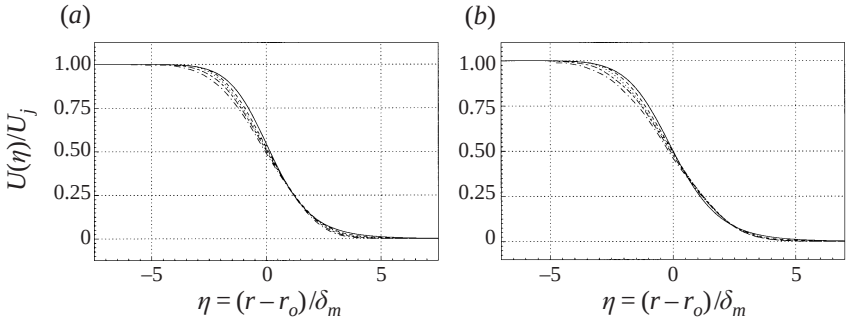

FIGURE 33. Self-similar like collapse of mean axial velocity data for (*a*) $M_c = 0.21$ case with curves at ——, $tU_j/r_o = 0.0$; – – –, 3.2; ·····, 5.1; — – —, 6.8; — · —, 8.5; and for (*b*) $M_c = 0.99$ case with curves at ——, $tU_j/r_o = 0.0$; – – –, 4.1; ·····, 8.1; — – —, 12.2; — · —, 16.3.

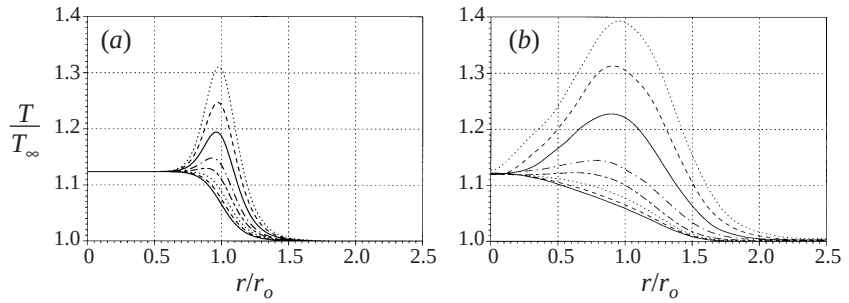

FIGURE 34. Mean temperature profiles for (*a*) the initial conditions and (*b*) at $\delta_m = 0.2r_o$ (from bottom to top): ——, $M_c = 0.21$; – – –, $M_c = 0.41$; ·····, $M_c = 0.59$; — – —, $M_c = 0.79$; — · —, $M_c = 0.99$; ——, $M_c = 1.29$; – – –, $M_c = 1.54$; ·····, $M_c = 1.80$.

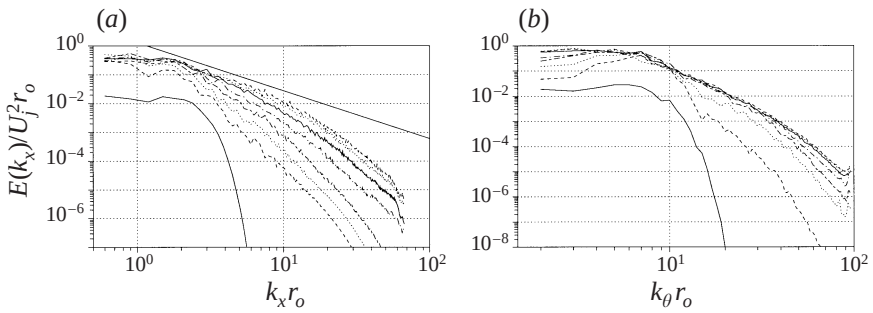

FIGURE 35. One-dimensional energy spectra for the $M_c = 0.99$ case at times (from bottom to top): ——, $tU_j/r_o = 0.0$; – – –, 3.1; ·····, 6.1; — – —, 9.2; — · —, 12.2; ——, 16.3; – – –, 19.3; ·····, 22.4. (*a*) Axial spectra; (*b*) azimuthal spectra. For reference, the straight line in (*a*) has $-5/3$ slope.

A.2. *Turbulence statistics*

A.2.1. *Energy spectra*

The evolution of the axial one-dimensional energy spectrum for the $M_c = 0.99$ case is shown in figure 35(*a*). This case is typical of all the runs. The spectral peak rapidly increases as energy is extracted from the mean flow and the spectrum slowly broadens as the turbulent energy cascade is established. Although the flow does not become statistically stationary, the spectrum evolves slowly at later times, suggesting that the

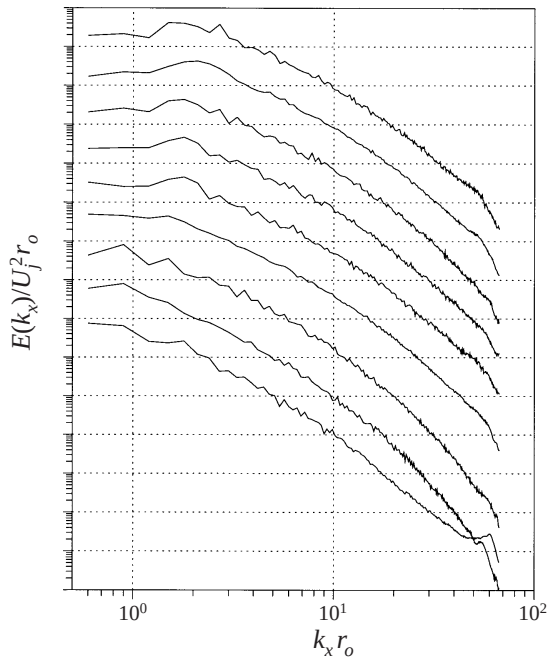

FIGURE 36. One-dimensional energy spectra in x at $\delta_m = 0.2r_o$. The spectra have been divided by factors of 10 so that the distinct curves can be seen. From top to bottom the curves are for $M_c = 0.10, 0.21, 0.41, 0.59, 0.79, 0.99, 1.29, 1.54$ and 1.80.

turbulence is well developed. These late times are studied in the greatest detail in this article. The θ-direction one-dimensional spectra (figure 35*b*) achieve a quasi-steady state in the low wavenumbers more rapidly than the x-direction spectra, but otherwise follow a similar development. The axial one-dimensional spectra for all cases at $\delta_m = 0.2r_o$ is shown in figure 36. All spectra are broadband with no discrete peaks of statistical significance. The wavenumber containing the highest energy decreases with increasing Mach number, which is consistent with longer wavelengths predicted by linear stability analysis. The anomaly at the highest wavenumbers of the $M_c = 1.80$ case is due to the difficulty in resolving very weak shocks that appear in the flow (see § 5.2).

A.2.2. *Two-point axial correlations*

It is important that the computational box be long enough for the turbulence to become decorrelated by its axial half-length. If this is not the case, the results may significantly depend upon the computational box size which would be unphysical. The spatial decorrelation of the present simulations is established via two-point correlations of velocity, density, and passive scalar concentration fluctuations at $r = r_o$ (figure 37). (The passive scalar is discussed and analysed in Freund, Moin & Lele 2000.) The correlations at all Mach numbers drop to a low value by the domain midpoint for all cases. It is clear that the streamwise correlation length is increasing with Mach number, which quantitatively reinforces the trends visualized in figure 25.

A.2.3. *Turbulence Mach number*

The turbulence Mach number, $M_t = (\overline{u'_x u'_x} + \overline{v'_r v'_r} + \overline{v'_\theta v'_\theta})^{1/2}/\bar{a}$, is an indicator of the level of compressibility of the turbulence. The evolution of the peak turbulence Mach number is plotted in figure 38 for all cases. After an initial adjustment, it increases

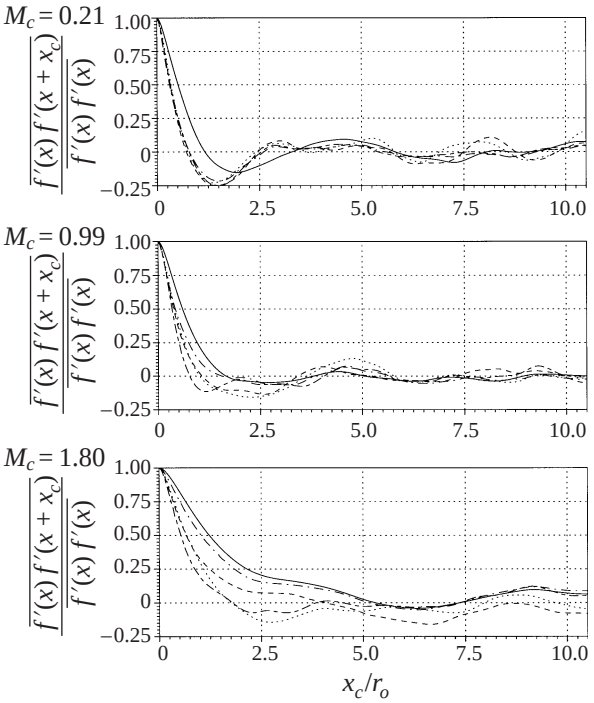

FIGURE 37. Two-point axial correlations with f representing ——, v_x'; – – –, v_r'; ·····, v_θ'; — — —, ρ'; — · —, scalar ξ'.

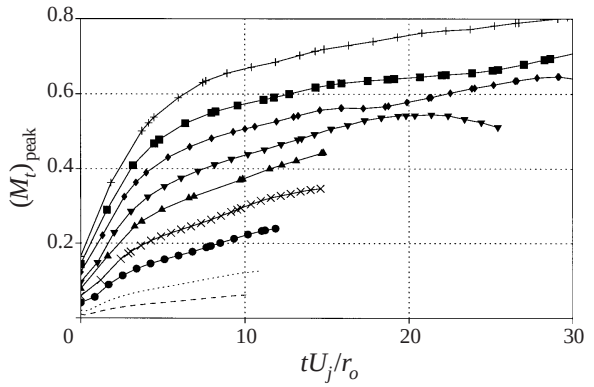

FIGURE 38. Evolution of the peak turbulence Mach number as the flow develops for – – –, $M_c = 0.2$; ·····, 0.21; ●, 0.41; ×, 0.59; ▲, 0.79; ▼, 0.99; ◆, 1.29; ■, 1.54; +, 1.80.

linearly in all cases, reaching as high as $M_t = 0.8$ in the $M_c = 1.80$ case. See § 6.3.2 for further discussion of turbulence Mach numbers.

A.2.4. *Reynolds stresses: comparison with plane mixing-layer experiments*

This flow has no laboratory counterpart and so there is no means of comparing it with an experiment under exactly the same conditions. However, since the present annular mixing-layer has mean velocity profile development and growth rate suppression similar to that observed in plane mixing-layer experiments, it is reasonable that

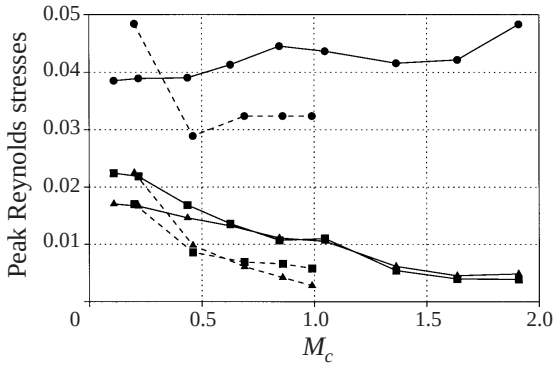

FIGURE 39. Peak Reynolds stresses from ——, the simulations at $\delta_m = 0.2r_o$ and from – – –, experimental plane mixing-layer measurements of Göebel & Dutton (1991). ●, $\overline{v'_x u'_x}/U_j^2$; ▲, $\overline{v'_r v'_r}/U_j^2$, ■, $\overline{v'_x v'_r}/U_j^2$ in the simulation results, and ●, $\overline{u'u'}/\Delta U^2$; ▲, $\overline{v'v'}/\Delta U^2$; ■, $-\overline{u'v'}/\Delta U^2$ in the experimental results which are naturally in terms of Cartesian velocities.

the Reynolds stresses should also be of similar magnitude and show similar trends with increasing compressibility. Peak Reynolds-stress data from the simulations are compared to the experimental data of Göebel & Dutton (1991) in figure 39 over a range of convective Mach numbers. The data show similar trends with increasing convective Mach number. Overall suppressions of the transverse and shear stresses, $\bar{\rho}\widetilde{v''_r v''_r}$ and $\bar{\rho}\widetilde{v''_x v''_r}$, are roughly the same, but the suppressions occur more slowly with convective Mach number in the present simulations. Note that the growth rate of the shear layer in the present simulations was also suppressed to the same degree, but this again occurred more slowly with increasing Mach number than in most experiments (figure 2). Geometrical differences between the annular and plane mixing layers may be responsible for this difference. For instance, Lau, Morris & Fisher (1979), who studied the early development of compressible round jets, also found that stresses were not suppressed as quickly as in the plane mixing layer of Göebel & Dutton. Another possible cause for the generally higher stresses in the present study is that the present mixing layer is in relatively early development. For example, Elliott & Samimy (1990) found that in a $M_c = 0.51$ plane mixing layer the turbulence is more intense before the flow achieves self-similarity. At their first measuring station, closest to the splitter plate, their Reynolds stresses were as much as 40% higher than their asymptotic downstream level. Not all experiments have observed the same invariance of the streamwise normal stress with increasing Mach numbers. Elliott & Samimy (1990) measured a decrease of this quantity with increasing Mach number in disagreement with Göebel & Dutton (1991), Urban & Mungal (1998), and the present simulations. Lau *et al.* (1979) found trends in general agreement with Elliott & Samimy for M_c values between 0.14 and 0.67.

Appendix B. Favre-averaged transport equations

The compressible Favre-averaged Reynolds-stress transport equations in cylindrical coordinates are given in equations (B 1)–(B 4). The terms are labelled and these labels are defined in table 3. For the present flow, some of the terms are negligible in all cases and these are indicated in the table. The axial and azimuthal homogeneity of

P	Production
MT	Mean flow transport (small)
TT	Turbulent transport
PDi	Pressure diffusion
VDi	Viscous diffusion (small)
VD	Viscous dissipation
PD	Pressure–strain rate redistribution
CR	Cylindrical coordinates redistribution
VW	Viscous work (small)
PW	Pressure work (small)

TABLE 3. Term label definitions for equations (B 1)–(B 4).

the flow has been invoked to simplify the expressions.

$$\begin{aligned}\frac{\partial\bar{\rho}\widetilde{v_x''v_x''}}{\partial t} = &-2\bar{\rho}\widetilde{v_x''v_r''}\frac{\partial\tilde{v}_x}{\partial r}\Bigg\}\mathrm{P} - \frac{1}{r}\frac{\partial r\bar{\rho}\tilde{v}_r\widetilde{v_x''v_x''}}{\partial r}\Bigg\}\mathrm{MT} - \frac{1}{r}\frac{\partial r\overline{\rho v_r''v_x''v_x''}}{\partial r}\Bigg\}\mathrm{TT}\\ &+\frac{2}{r}\frac{\partial r\overline{\tau_{xr}'v_x''}}{\partial r}\Bigg\}\mathrm{VDi} - 2\overline{\tau_{xx}'\frac{\partial v_x''}{\partial x}} - 2\overline{\tau_{xr}'\frac{\partial v_x''}{\partial r}} - 2\overline{\tau_{x\theta}'\frac{1}{r}\frac{\partial v_x''}{\partial\theta}}\Bigg\}\mathrm{VD}\\ &+2\overline{p'\frac{\partial v_x''}{\partial x}}\Bigg\}\mathrm{PS} + 2\overline{v_x''}\frac{1}{r}\frac{\partial r\bar{\tau}_{xr}}{\partial r}\Bigg\}\mathrm{VW},\end{aligned} \tag{B 1}$$

$$\begin{aligned}\frac{\partial\bar{\rho}\widetilde{v_r''v_r''}}{\partial t} = &-2\bar{\rho}\widetilde{v_r''v_r''}\frac{\partial\tilde{v}_r}{\partial r}\Bigg\}\mathrm{P} - \frac{1}{r}\frac{\partial r\bar{\rho}\tilde{v}_r\widetilde{v_r''v_r''}}{\partial r}\Bigg\}\mathrm{MT} - \frac{1}{r}\frac{\partial r\overline{\rho v_r''v_r''v_r''}}{\partial r}\Bigg\}\mathrm{TT}\\ &-\frac{2}{r}\frac{\partial r\overline{p'v_r''}}{\partial r}\Bigg\}\mathrm{PDi} + \frac{2}{r}\frac{\partial r\overline{\tau_{rr}'v_r''}}{\partial r}\Bigg\}\mathrm{VDi}\\ &-2\overline{\tau_{rx}'\frac{\partial v_r''}{\partial x}} - 2\overline{\tau_{rr}'\frac{\partial v_r''}{\partial r}} - 2\overline{\tau_{r\theta}'\frac{1}{r}\frac{\partial v_r''}{\partial\theta}} - 2\overline{\frac{v_r''\tau_{\theta\theta}}{r}}\Bigg\}\mathrm{VD}\\ &+2\overline{p'\frac{1}{r}\frac{\partial rv_r''}{\partial r}}\Bigg\}\mathrm{PS} + \frac{2}{r}\overline{\rho v_r''v_\theta''v_\theta''}\Bigg\}\mathrm{CR} + \overline{v_r''}\frac{2}{r}\frac{\partial r\bar{\tau}_{rr}}{\partial r}\Bigg\}\mathrm{VW} - 2\overline{v_r''}\frac{\partial\bar{p}}{\partial r}\Bigg\}\mathrm{PW},\end{aligned} \tag{B 2}$$

$$\begin{aligned}\frac{\partial\bar{\rho}\widetilde{v_\theta''v_\theta''}}{\partial t} = &-\frac{2}{r}\bar{\rho}\tilde{v}_r\widetilde{v_\theta''v_\theta''}\Bigg\}\mathrm{P} - \frac{1}{r}\frac{\partial r\bar{\rho}\tilde{v}_r\widetilde{v_\theta''v_\theta''}}{\partial r}\Bigg\}\mathrm{MT} - \frac{1}{r}\frac{\partial r\overline{\rho v_r''v_\theta''v_\theta''}}{\partial r}\Bigg\}\mathrm{TT}\\ &+\frac{2}{r}\frac{\partial r\overline{\tau_{r\theta}'v_\theta''}}{\partial r}\Bigg\}\mathrm{VDi} - 2\overline{\tau_{x\theta}'\frac{\partial v_\theta''}{\partial x}} - 2\overline{\tau_{r\theta}'\frac{\partial v_\theta''}{\partial r}} - 2\overline{\tau_{\theta\theta}'\frac{1}{r}\frac{\partial v_r''}{\partial\theta}} + 2\overline{\frac{v_\theta''\tau_{\theta r}}{r}}\Bigg\}\mathrm{VD}\\ &+2\overline{p'\frac{1}{r}\frac{\partial v_\theta''}{\partial\theta}}\Bigg\}\mathrm{PS} - \frac{2}{r}\overline{\rho v_\theta''v_\theta''v_r''}\Bigg\}\mathrm{CR} + \overline{v_\theta''}\frac{2}{r}\frac{\partial r\bar{\tau}_{\theta r}}{\partial r}\Bigg\}\mathrm{VW},\end{aligned} \tag{B 3}$$

$$\frac{\partial \bar{\rho}\widetilde{v_x''v_r''}}{\partial t} = \left.-\bar{\rho}\widetilde{v_r''v_r''}\frac{\partial \tilde{v}_x}{\partial r} - \bar{\rho}\widetilde{v_x''v_r''}\frac{\partial \tilde{v}_r}{\partial r}\right\}\mathrm{P} - \left.\frac{1}{r}\frac{\partial r\bar{\rho}\tilde{v}_r\widetilde{v_x''v_r''}}{\partial r}\right\}\mathrm{MT} - \left.\frac{1}{r}\frac{\partial r\overline{\rho v_r''v_x''v_r''}}{\partial r}\right\}\mathrm{TT}$$

$$\left.-\frac{1}{r}\frac{\partial r\overline{p'v_x''}}{\partial r}\right\}\mathrm{PDi} + \left.\frac{1}{r}\frac{\partial}{\partial r}\left[r\overline{\tau'_{xr}v_r''} + r\overline{\tau'_{rr}v_x''}\right]\right\}\mathrm{VDi} + \left.\overline{p'\left(\frac{\partial v_r''}{\partial x} + \frac{1}{r}\frac{\partial rv_x''}{\partial r}\right)}\right\}\mathrm{PS}$$

$$\left.-\overline{\tau'_{xx}\frac{\partial v_r''}{\partial x}} - \overline{\tau'_{xr}\frac{\partial v_r''}{\partial r}} - \overline{\tau'_{x\theta}\frac{1}{r}\frac{\partial v_r''}{\partial \theta}} - \overline{\tau'_{rx}\frac{\partial v_x''}{\partial x}} - \overline{\tau'_{rr}\frac{\partial v_x''}{\partial r}} - \overline{\tau'_{r\theta}\frac{1}{r}\frac{\partial v_x''}{\partial \theta}} - \overline{\frac{v_x''\tau_{\theta\theta}}{r}}\right\}\mathrm{VD}$$

$$\left.+\frac{1}{r}\overline{\rho v_x''v_\theta''v_\theta''}\right\}\mathrm{CR} + \left.\overline{v_r''}\frac{1}{r}\frac{\partial r\bar{\tau}_{xr}}{\partial r} + \overline{v_x''}\frac{1}{r}\frac{\partial r\bar{\tau}_{rr}}{\partial r}\right\}\mathrm{VW} - \left.\overline{v_x''}\frac{\partial \bar{p}}{\partial r}\right\}\mathrm{PW}. \tag{B 4}$$

Most of the terms have exact analogies in incompressible flow, but VW and P do not. They act to exchange energy between mean internal and the turbulent kinetic energy and their origin is essentially an artifact of the decomposition used by Favre (1969) (see also Lele 1994). However, this particular decomposition is not unique. It is also possible, and perhaps more instructive in some situations, to use another self-consistent formulation in which similar terms act to exchange energy between turbulent kinetic energy and mean kinetic energy. This approach is favoured by Huang, Coleman & Bradshaw (1995). The terms in question are insignificant in the present flow at all Mach numbers and therefore the particular decomposition is immaterial.

The pressure terms in (B 1)–(B 4) were split into separate pressure–strain-rate and pressure diffusion terms. They may also be combined into velocity–pressure-gradient terms which are, for (B 1)–(B 4), respectively,

$$\overline{p'\frac{\partial v_x''}{\partial x}} = -\overline{v_x''\frac{\partial p'}{\partial x}}, \tag{B 5}$$

$$\overline{\frac{p'}{r}\frac{\partial rv_r''}{\partial r}} - \frac{1}{r}\frac{\partial r\overline{p'v_r''}}{\partial r} = -\overline{v_r''\frac{\partial p'}{\partial r}}, \tag{B 6}$$

$$\overline{\frac{p'}{r}\frac{\partial v_\theta''}{\partial \theta}} = -\overline{\frac{v_r''}{r}\frac{\partial p'}{\partial \theta}}, \tag{B 7}$$

$$\overline{p'\left(\frac{\partial v_r''}{\partial x} + \frac{1}{r}\frac{\partial rv_x''}{\partial r}\right)} - \frac{1}{r}\frac{\partial r\overline{p'v_x''}}{\partial r} = -\overline{v_r''\frac{\partial p'}{\partial x}} - \overline{v_x''\frac{\partial p'}{\partial r}}. \tag{B 8}$$

The split was made to differentiate the effects of transport from intercomponent redistribution and was motivated by the fact that these are two distinct physical effects. Although such a decomposition is neither unique nor necessarily the best for all flows (Mansour, Kim & Moin 1988), it is often used.

A transport equation for the turbulent kinetic energy is formed by summing (B 1)–(B 3). The only new term is the pressure dilatation correlation formed from the sum of the pressure–strain-rate correlations:

$$\overline{p'\left(\frac{\partial v_x''}{\partial x} + \frac{1}{r}\frac{\partial rv_r''}{\partial r} + \frac{1}{r}\frac{\partial v_\theta''}{\partial \theta}\right)}. \tag{B 9}$$

REFERENCES

Barre, S., Quine, C. & Dussauge, J. P. 1994 Compressibility effects on the structure of supersonic mixing layers: experimental results. *J. Fluid Mech.* **259**, 47–78.

Birch, S. L. & Eggers, J. M. 1972 A critical review of the experimental data on turbulent shear layers. NASA SP 321.

Blaisdell, G. A., Mansour, N. N. & Reynolds, W. C. 1993 Compressibility effects on the growth and structure of homogeneous turbulent shear flow. *J. Fluid Mech.* **256**, 443–485.

Bogdanoff, D. W. 1983 Compressibility effects in turbulent shear layers. *AIAA J.* **21**, 926–927.

Bradshaw, P. 1977 Compressible turbulent shear layers. *Ann. Rev. Fluid Mech.* **9**, 33–54.

Bradshaw, P. 1996 Turbulence in compressible flow – physics and modeling. *J. Japan Soc. Fluid Mech.* **15**, 354–363.

Breidenthal, R. 1990 The sonic eddy – a model for compressible turbulence. *AIAA Paper* 90-0495.

Broadwell, J. E. & Breidenthal, R. E. 1982 A simple model of mixing and chemical reaction in a turbulent shear layer. *J. Fluid Mech.* **125**, 397–410.

Brown, G. L. & Roshko, A. 1974 On density effects and large structure in turbulent mixing layers. *J. Fluid Mech.* **64**, 775–816.

Burr, R. F. & Dutton, J. C. 1990 Numerical modelling of compressible reacting shear layers. *AIAA Paper* 90-1463.

Chinzei, N., Masuya, G., Komuro, T., Murakami, A. & Kudou, K. 1986 Spreading of two-stream supersonic turbulent mixing layers. *Phys. Fluids* **29**, 1345–1347.

Clemens, N. T. & Mungal, M. G. 1992 Two- and three-dimensional effects in the supersonic mixing layer. *AIAA J.* **30**, 973–981.

Clemens, N. T. & Mungal, M. G. 1995 Large-scale structure and entrainment in the supersonic mixing layer. *J. Fluid Mech.* **284**, 171–216.

Clemens, N. T. & Paul, P. H. 1995 Scalar measurements in compressible axisymmetric mixing layers. *Phys. Fluids* **7**, 1071–1081.

Day, M. J., Reynolds, W. C. & Mansour, N. N. 1998 The structure of the compressible reacting mixing layer: insights from linear stability analysis. *Phys. Fluids* **10**, 993–1007.

Dimotakis, P. E. 1989 Turbulent shear layer mixing with fast chemical reactions. *Turbulent Reacting Flows* **125**, 397–410.

Dimotakis, P. E. 1991 Turbulent free shear layer mixing and combustion. *Prog. Astronaut. Aeronaut.* **137**, 265–340.

Elliott, G. & Samimy 1990 Compressibility effects in free shear layers. *Phys. Fluids* A **2**, 1231–1239.

Favre, A. 1969 Statistical equations of turbulent gases. In *Problems of Hydrodynamics and Continuum Mechanics,* pp. 231–266. SIAM Philadelphia.

Fourguette, D. C., Mungal, M. G. & Dibble, R. W. 1991 Time evolution of the shear layer of a supersonic axisymmetric jet at matched conditions. *AIAA J.* **29**, 1123–1130.

Freund, J. B., Moin, P. & Lele, S. K. 1997 Compressibility effects in a turbulent annular mixing layer. *Tech. Rep.* TF-72, Stanford University, Mechanical Engineering, Flow Physics and Computation Division.

Freund, J. B., Moin, P. & Lele, S. K. 2000 Compressibility effects in a turbulent annular mixing layer. Part 2. Mixing of a passive scalar. *J. Fluid Mech.* **421**, 269–292.

Göebel, S. G. & Dutton, J. C. 1991 Experimental study of compressible turbulent mixing layers. *AIAA J.* **29**, 538–546.

Gutmark, E. J., Schadow, K. C. & Yu, K. H. 1995 Mixing enhancement in supersonic free shear flows. *Ann. Rev. Fluid Mech.* **27**, 375–417.

Hall, J. L., Dimotakis, P. E. & Rosemann, H. 1993 Experiments in nonreacting compressible shear layers. *AIAA J.* **31**, 2247–2254.

Huang, P. G., Coleman, G. N. & Bradshaw, P. 1995 Compressible turbulent channel flows: DNS results and modelling. *J. Fluid Mech.* **305**, 185–218.

Knight, D. 1997 Numerical simulation of compressible turbulent flows using the Reynolds-averaged Navier–Stokes equations. AGARD/VKI Special Course on Turbulence in Compressible Flows, AGARD R-819.

Kraichnan, R. H. 1956 Pressure field within homogeneous anisotripic turbulence. *J. Acoust. Soc. Am.* **28**, 64–72.

Lau, J. C., Morris, P. J. & Fisher, M. J. 1979 Measurements in subsonic and supersonic free jets using a laser velocimeter. *J. Fluid Mech.* **93**, 1–27.

LEE, S., LELE, S. K. & MOIN, P. 1991 Eddy shocklets in decaying compressible turbulence. *Phys. Fluids* A **3**, 657–664.

LELE, S. K. 1989 Direct numerical simulation of compressible free shear flows. *AIAA Paper* 89-0374.

LELE, S. K. 1992 Compact finite difference schemes with spectral-like resolution. *J. Comput. Phys.* **103**, 16–42.

LELE, S. K. 1994 Compressibility effects on turbulence. *Ann. Rev. Fluid Mech.* **26**, 211–254.

LIGHTHILL, M. J. 1955 The effect of compressibility on turbulence. In *Gas Dynamics of Cosmic Clouds, Symp. Proc., Cambridge, England, 6–11 July 1953*. North-Holland.

MANSOUR, N. N., KIM, J. & MOIN, P. 1988 Reynolds-stress and dissipation-rate budgets in a turbulent channel flow. *J. Fluid Mech.* **194**, 15–44.

MESSERSMITH, N. L. & DUTTON, J. C. 1996 Characteristic features of large structures in compressible mixing layers. *AIAA J.* **34**, 1814–1821.

MORKOVIN, M. V. 1961 Effects of compressibility on turbulent flows. In *Mécanique de la Turbulence* (ed. A. Favre), pp. 367–380. CNRS.

MOSER, R. D. & ROGERS, M. M. 1993 The three-dimensional evolution of a plane mixing layer: pairings and transition to turbulence. *J. Fluid Mech.* **247**, 275–320.

PAPAMOSCHOU, D. 1995 Evidence of shocklets in a counterflow supersonic shear layer. *Phys. Fluids* **7**, 233–235.

PAPAMOSCHOU, D. 1997 Mach wave elimination in supersonic jets. *AIAA J.* **36**, 1604–1611.

PAPAMOSCHOU, D. & ROSHKO, A. 1988 The compressible turbulent shear layer: an experimental study. *J. Fluid Mech.* **197**, 453–477.

PASSOT, T. & POUQUET, A. 1987 Numerical simulation of compressible homogeneous flows in the turbulent regime. *J. Fluid Mech.* **181**, 441–466.

RAGAB, S. A. & WU, J. L. 1990 Linear instability in two-dimensional compressible mixing layers. *Phys. Fluids* A **1**, 975–966.

RISTORCELLI, J. R. & BLAISDELL, G. A. 1997 Consistent initial conditions for the DNS of compressible turbulence. *Phys. Fluids* **9**, 4–6.

ROGERS, M. M. & MOSER, R. D. 1994 Direct simulation of a self-similar turbulent mixing layer. *Phys. Fluids* **6**, 903–923.

SAMIMY, M. & ELLIOTT, G. S. 1990 Effects of compressibility on the characteristics of free shear layers. *AIAA J.* **28**, 439–445.

SAMIMY, M., REEDER, M. F. & ELLIOTT, G. S. 1992 Compressibility effects on large structures in free shear flows. *Phys. Fluids* A **4**, 1251–1258.

SANDHAM, N. D. & REYNOLDS, W. C. 1990 Compressible mixing layer: linear theory and direct simulation. *AIAA J.* **28**, 618–624.

SANDHAM, N. & REYNOLDS, W. 1991 Three-dimensional simulations of large eddies in the compressible mixing layer. *J. Fluid Mech.* **224**, 133–158.

SANDHAM, N. D. & YEE, H. C. 1989 A numerical study of a class of TVD schemes for compressible mixing layers. *NASA Tech. Rep.* 102194.

SARKAR, S. 1995 The stabilizing effect of compressibility in turbulent shear flow. *J. Fluid Mech.* **282**, 163–186.

SARKAR, S., ERLEBACHER, G. & HUSSAINI, M. Y. 1991*a* Direct simulation of compressible turbulence in a shear flow. *Theoret. Comput. Fluid Dyn.* **2**, 291–305.

SARKAR, S., ERLEBACHER, G., HUSSAINI, M. Y. & KREISS, H. O. 1991*b* The analysis and modelling of dilatational terms in compressible turbulence. *J. Fluid Mech.* **227**, 473–493.

SIMONE, A., COLEMAN, G. N. & MANSOUR, N. N. 1997 The effect of compressibility on turbulent shear flow: a rapid-distortion-theory and direct-numerical simulation study. *J. Fluid Mech.* **330**, 307–338.

URBAN, W. D. & MUNGAL, M. G. 1998 A PIV study of compressible shear layers. *9th Intl Symp. on Applications of Laser Techniques to Fluid Mechanics, Lisbon, Portugal.*

VREMAN, B., KUERTEN, H. & GEURTS, B. 1995 Shocks in DNS of the three-dimensional mixing layer. *Presented at 10th Symp. on Turbulent Shear Flows.*

VREMAN, A. W., SANDHAM, N. & LUO, K. H. 1996 Compressible mixing layer growth rate and turbulence characteristics. *J. Fluid Mech.* **320**, 235–258.

ZEMAN, O. 1990 Dilatational dissipation: the concept and application in modeling compressible mixing layers. *Phys. Fluids* A **2**, 178–188.